COMPUTATIONAL OPTIMIZATION OF TRANSCATHETER AORTIC VALVE LEAFLET DESIGN

A Thesis
Presented to
The Academic Faculty

by

Kyle Murdock

In Partial Fulfillment
of the Requirements for the Degree
Master of Science in the
School of Biomedical Engineering

Georgia Institute of Technology
August 2016

COMPUTATIONAL OPTIMIZATION OF TRANSCATHETER AORTIC VALVE LEAFLET DESIGN

Approved by:

Dr. Wei Sun, Advisor
School of Biomedical Engineering
Georgia Institute of Technology

Dr. Eric Sarin
School of Medicine
Emory University

Dr. Yan Wang
School of Mechanical Engineering
Georgia Institute of Technology

Dr. Muralidhar Padala
School of Biomedical Engineering
Georgia Institute of Technology

Date Approved: July 14, 2016

ACKNOWLEDGEMENTS

I would like to thank my advisor, Dr. Wei Sun, for his continued support through my graduate education. I would also like to thank all the members of the Tissue Mechanics Laboratory that I have had the pleasure of knowing: Dr. Caitlin Martin, Dr. Kewei Li, Dr. Thuy Pham, Dr. Qian Wang, Dr. Wenbin Mao, Andres Caballero, Minliang Liu, Dr. Liang Liang, Dr. Haofei Liu, and Fatiesa Sulejmani. Special thanks to Fatiesa and Michael Moon for their help with the collection of experimental data. I would especially like to thank my committee members: Dr. Muralidhar Padala, Dr. Eric Sarin, and Dr. Yan Wang for their support and guidance.

TABLE OF CONTENTS

Page

ACKNOWLEDGEMENTS……iii

LIST OF TABLES…….. vii

LIST OF FIGURES……... viii

SUMMARY…… xii

1 Introduction……...1

1.1 The Heart……... 1

1.2 The Aortic Valve……2

1.2.1 Aortic Valve Leaflets 3

1.2.2 Aortic Valve Calcification 4

1.3 Aortic Valve Replacement……5

1.3.1 Surgical Aortic Valve Replacement..... 6

1.3.2 Transcatheter Aortic Valve Replacement 6

1.4 Transcatheter Aortic Valve Design……7

1.4.1 Design Considerations 8

1.4.2 Current Device Generations..... 8

1.4.3 Device Degeneration and Failure..... 10

1.5 Design Optimization and Device Safety……..11

1.5.1 Device Optimization 12

1.5.2 Robustness and Reliability..... 12

1.6 Project Objective……..13

1.6.1 Specific Aim 1 13

1.6.2 Specific Aim 2 13

2 Constitutive modeling of animal pericardia……14
2.1 Collagenous Soft Tissue…….. 14
2.1.1 Structure and Function 14
2.1.2 Mechanical Characterization of Soft Tissue 15
2.1.3 Modeling Soft Tissue Mechanics 17
2.2 Experimental Testing and Modeling……20
2.2.1 Material Preparation 21
2.2.2 Biaxial Testing 21
2.2.3 Cantilever Bending 22
2.2.4 Inverse FEA 23
2.2.5 FEA Flexure Optimization Framework 25
2.2.6 Valve Modeling 26
2.3 Pericardium Flexure and TAV Modeling…… 27
2.3.1 Biaxial Testing 27
2.3.2 Flexural Testing 28
2.3.3 Inverse FEA 29
2.4 Discussion…… 33
2.4.1 Mechanical Testing Modalities 34
2.4.2 Tissue Structure and Function 35
2.4.3 Implications for Valve Design 36
2.4.4 Study Limitations 36
3 A Computational Framework for Design of Tanscatheter Aortic Valve Leaflets…….. 38
3.1 Design Optimization, Robustness, and Uncertainty…… 38
3.1.1 Strategies for Optimization 39
3.1.2 Strategies for Robustness and Reliability 39

3.2 TAV Leaflet Modeling…… 41
3.2.1 Leaflet Geometry Parameterization 41
3.2.2 Virtual Assembly 43
3.2.3 Finite Element Analysis 46
3.2.4 TAV Design Space 48
3.3 Parameterization Study and Combinatorial Design……51
3.4 TAV Leaflet Optimization……...59
3.5 TAV Leaflet Robustness……. 63
3.6 Limitations and Future Directions……... 69
4 Conclusions……71
4.1 Material Properties……...71
4.2 TAV Leaflet Design……71
APPENDIX A……73
REFERENCES…….. 77

LIST OF TABLES

Page

Table 1. Material model parameters from curve fitting mean biaxial responses. 28

Table 2. Material parameters obtained after bending optimization and biaxial re-fitting. 31

Table 3. Design comparison of nominal and optimized leaflet geometries. 61

Table 4. Design parameters from robust optimization. 64

LIST OF FIGURES

Page

Figure 1. Artistic rendition of a normal heart, courtesy of www.interactive-biology.com 1

Figure 2. Representative pressure and volume waveforms during diastole and systole, courtesy of www.cvphysiology.com..... 2

Figure 3. Anatomy of AV leaflet inside a dissected aortic annulus, taken from Kasel [1]. 3

Figure 4. Typical patterns of calcium deposition in native aortic valves commonly develop circumferentially, across the belly (A) or radially, along the attachment edge (B) [6]..... 5

Figure 5. Carpentier-Edwards PERIMOUNT aortic valve bioprosthesis. (courtesy of www.edwards.com) 6

Figure 6. Current generations of TAV designs, adapted from Walther et al. [15]. 9

Figure 7. Representative evolution of percutaneous aortic valve design, taken from Fanning et al. [16]. 10

Figure 8. Soft tissue stress-strain response is associated with collagen fiber deformation [34]. 15

Figure 9. Biaxial setup (left), where tissue is loaded using sutures (right). 17

Figure 10. Representative sequence of image acquisition (A), thresholding (B), and digitization (C). 23

Figure 11. FEA bending (a) compared to experimental fit parameters (b). Side-by-side comparison of deflection curves (c). 24

Figure 12. Optimization scheme for identifying appropriate material parameters. 25

Figure 13. Planar images are extracted from Abaqus (A), converted to binary (B), and GOA is calculated (C). 26

Figure 14. Constitutive model fitting of average PPK deformation (only 1:1 loading protocol shown), where 11 and 22 are the preferred- and cross-fiber directions, respectively. 27

Figure 15. Average deflection curves for bovine (A) and porcine (B) tissues. 28

Figure 16. Average experimental deflection curves (blue) compared to FEA deflection resulting from the original biaxial parameters (black) and bending-

optimized parameters (red). 125 mg (left) and 56 mg (right) weights were used for thick (top) and thin (bottom) bovine pericardium. 29

Figure 17. Average experimental deflection curves (blue) compared to FEA deflection resulting from the original biaxial parameters (black) and bending-optimized parameters (red). 45mg (left) and 19mg (right) weights were used for thick (top) and thin (bottom) porcine pericardium. 30

Figure 18. Influence of CC on the average coefficient of determination. 31

Figure 19. Comparison of undeformed (A) and deformed (B) valve deformation with leaflet midline nodes highlighted in red. Midline deflection curves (C, D) after systolic pressurization, $\Delta p = 4mmHg$. Comparison of leaflet models using biaxial and flexure-derived parameters (C). Evaluation of select models with parameters derived from biaxial-only data (solid lines) and biaxial-flexure data (dashed lines). 32

Figure 20. Relationship between GOA and pressure for all four tissue groups (A). Comparison of material coefficients for thin groups (B) 33

Figure 21. Flowchart of computational study of TAV leaflet design. 41

Figure 22. Geometric characterization of TAV leaflet with 2D shape parameter, a, and SSL. 42

Figure 23. Effect of 3D shape parameter, b, on attachment edge shape. Black lines represent inner stent boundary. 43

Figure 24. Illustration of TPS leaflet re-meshing. After specifying a template mesh (A), updated boundary nodes (white dots) are used to generate the target mesh (B). 44

Figure 25. Material orientation axes (A) were defined in the radial (blue) and circumferential (red) directions. Node and element sets (B) were defined across the leaflet to monitor stress and contact distribution. 45

Figure 26. Oblique (A) and top (B) view of boundary conditions used to create an elliptical boundary. The red and yellow dashed lines represent the long and short axis, respectively. 47

Figure 27. Normal distributions of eccentricity values to represent likelihood of elliptical deployment. 48

Figure 28. ASA optimization framework layout (top) and breakdown of component outputs (bottom) 49

Figure 29. Robust-optimization arrangement. TAV leaflets are generated as previously described (left), elliptical boundaries are generated (right), and diastolic

pressurization is performed. The mean and standard deviation of MPS is output from the Six Sigma module to the Optimization component. 50

Figure 30. Distribution of stress in the M-regions was strongly correlated with the maximum principles stress of the entire leaflet. The data trendline is drawn in green..... 52

Figure 31. Effect of SSL on total leaflet MPS. 53

Figure 32. Effect of SSL on stress distribution in the M-region. Stress distribution, M_{std}, (A) was influenced by SSL in a material dependent manner..... 54

Figure 33. Effect of 2D leaflet shape on contact area (A) and stress concentrations (B), only BP shown. 55

Figure 34. Impact of 3D attachment shape on leaflet-to-leaflet contact area (A) and stress concentrations (B). 56

Figure 35. Interaction between *b* and SSL on leaflet MPS. 57

Figure 36. Interaction effect between *a* and SSL on maximum principle stress. 58

Figure 37. Parallel coordinate graph of input parameters and key output metrics. C_{std} and M_{std} is the standard deviation of contact area in the T-regions and stress in the M-regions, respectively. Output values only reported from BP leaflets. 59

Figure 38. Search history of parameters a (A) and b (B) demonstrated convergence of optimization (PP material model). 60

Figure 39. History of SSL during leaflet optimization (PP material model). 61

Figure 40. Comparison of nominal (A, C) and optimized (B, D) designs for bovine (top) and porcine (bottom) leaflet materials under diastolic pressurization. 62

Figure 41. Response surface plot of 2D leaflet surface area (cm^2), attachment edge shape parameter, and max principle stress (PSI) using BP material parameters. The design resulting in lowest MPS is highlighted in pink. 63

Figure 42. Comparison of valve design performance under elliptical deployment distributions. Orange and gray bars represent the ASA-optimized and robustness-optimized designs, respectively. Error bars represent standard deviation and asterisks indicate significant differences, $p < 0.05$..... 65

Figure 43. Optimal leaflet designs under E_0 (A), E_3 (B), E_5 (C) eccentricity distributions. 66

Figure 44. Contact area (left) and MPE (right) for E_3 (top) and E_5 (bottom) optimal leaflet designs..... 67

Figure 45. Representative valve design under elliptical closure (e = 0.3). MPS of the TAV is correlated with M-region stress distribution in the non-collapsing leaflet (right) and collapsing leaflet (left). 68

Figure 46. Effect of leaflet contact distribution on stress concentration along the M-region (M_{std}) of the non-collapsing leaflet under E_5 eccentricity optimization. Linear trendline shown in green. 69

Figure 47. Average biaxial response for thick bovine pericardium in the preferred-fiber (X1) and cross-fiber (X2) directions. 73

Figure 48. Average biaxial response for thin bovine pericardium in the preferred-fiber (X1) and cross-fiber (X2) directions. 73

Figure 49. Average biaxial response for thick porcine pericardium in the preferred-fiber (X1) and cross-fiber (X2) directions. 74

Figure 50. Average biaxial response for thin porcine pericardium in the preferred-fiber (X1) and cross-fiber (X2) directions. 74

Figure 51. ASA optimization history (top) and relationship between leaflet MPS and M-region stress distribution (bottom) with bovine pericardia properties, trendline shown in green. 75

Figure 52. ASA optimization history (top) and relationship between leaflet MPS and M-region stress distribution (bottom) with porcine pericardia properties, trendline shown in green. 76

SUMMARY

Transcatheter aortic valve (TAV) replacement is now the standard of care treatment for aortic stenosis in high-risk patients. There has been a recent push in the industry to develop smaller profile TAVs to make this treatment a safe and effective alternative to valve surgery in an even wider spectrum of patients. Smaller devices requiring thinner leaflets may come with the tradeoff of reduced durability. However, the impacts of different TAV leaflet materials and valve designs on TAV function and durability, particularly under non-ideal deployment conditions, have not been thoroughly assessed. By combining material modeling and geometric parameterization of valve leaflets, performance and safety of TAV devices can be comprehensively evaluated. The objectives of this study were to employ constitutive modeling tools to describe the material properties of pericardial tissues, and then to implement them in the development of a computational framework for exploring the impacts of leaflet material and design on TAV function.

The mechanical properties of pericardial tissue have not been well characterized, particularly under flexure, which is an important mode of deformation for native and bioprosthetic heart valves. Pericardia material models were implemented in finite element simulations of valve deformation and directly compared. The impact of TAV leaflet material and geometry on mechanical stress was closely examined and fundamental relationships between design characteristics and leaflet deformation were established. Eccentric TAV expansion was modeled and optimization tools were employed to identify leaflet geometries which minimize stress during mechanical loading to increase durability. The results from these studies may offer scientific rationale for the design of durable and robust next-generation TAV devices.

1 INTRODUCTION

1.1 The Heart

The heart is responsible for driving blood flow through the body. As seen in Figure 1, the heart is composed of four chambers and four valves. Chambers pump blood in a specific direction and valves ensure unidirectional blood flow.

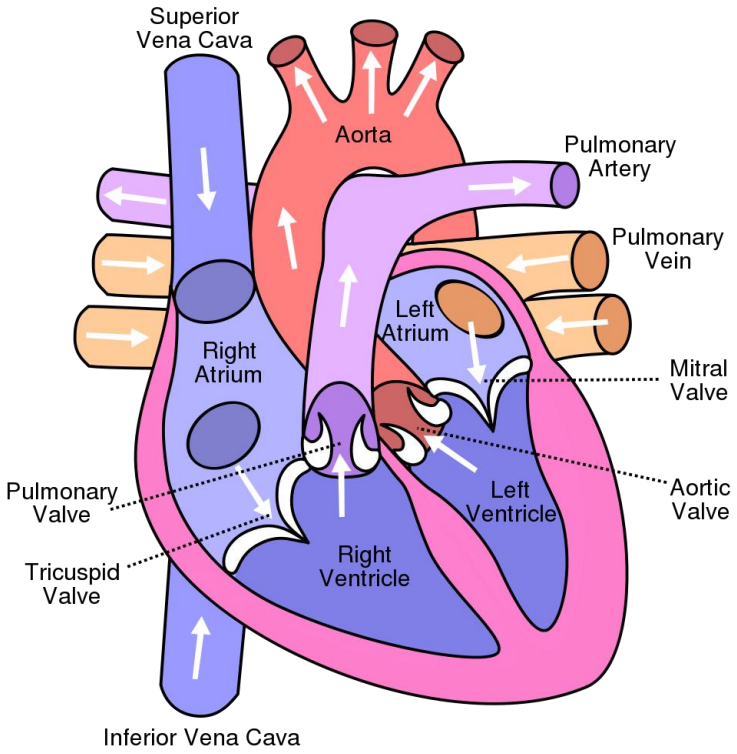

Figure 1. Artistic rendition of a normal heart, courtesy of www.interactive-biology.com

Oxygenated blood enters the left atrium via pulmonary veins and the mitral valve allows blood to fill the left ventricle (LV) during diastole. The myocardial muscle surrounding the left ventricle contracts, dramatically increasing LV pressure. Pressure inside the

cardiovascular system drives blood flow. A typical pressure waveform through a cardiac cycle is illustrated in Figure 2.

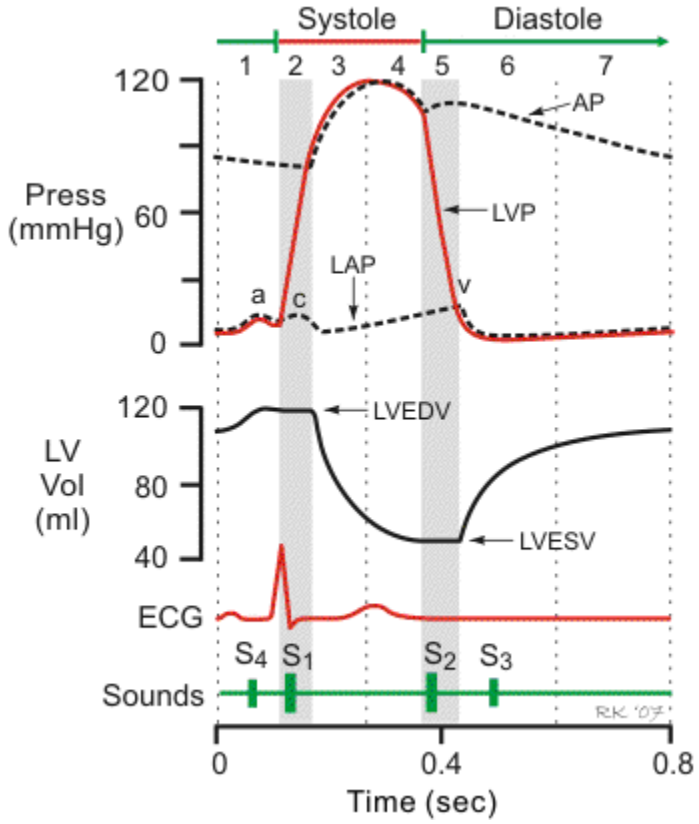

Figure 2. Representative pressure and volume waveforms during diastole and systole, courtesy of www.cvphysiology.com

Systolic ejection is followed by a myocardial relaxation phase where blood is pooled in the LV again. Aortic pressure is approximately 80 mmHg at the beginning of systole and reaches approximately 120 mmHg near diastole. The net pressure difference across the aortic valve, i.e. transvalvular pressure gradient, during systole is usually very low, yet large enough to cause aortic valve leaflets to bend open.

1.2 The Aortic Valve

The aortic valve (AV) allows unidirectional blood flow from the left ventricle to the aorta. The aortic valve opens during ventricular systole and closes during diastole.

During systole, contraction of left ventricular muscle drives blood flow through the aortic valve towards the coronary arteries and aorta. The aortic valve consists of 3 symmetric, thin leaflets. A rapid shift in transvalvular pressure gradient causes AV leaflets to quickly bend such that the valve is opened.

1.2.1 Aortic Valve Leaflets

AV leaflets are thin, avascular structures whose pressure-driven deformation allows for unidirectional blood flow to the aorta. The left coronary leaflet, right coronary leaflet, and non-coronary leaflets are named for their proximity to their respective coronary artery ostium. An illustration of native AV leaflets within the aortic root is displayed in Figure 3.

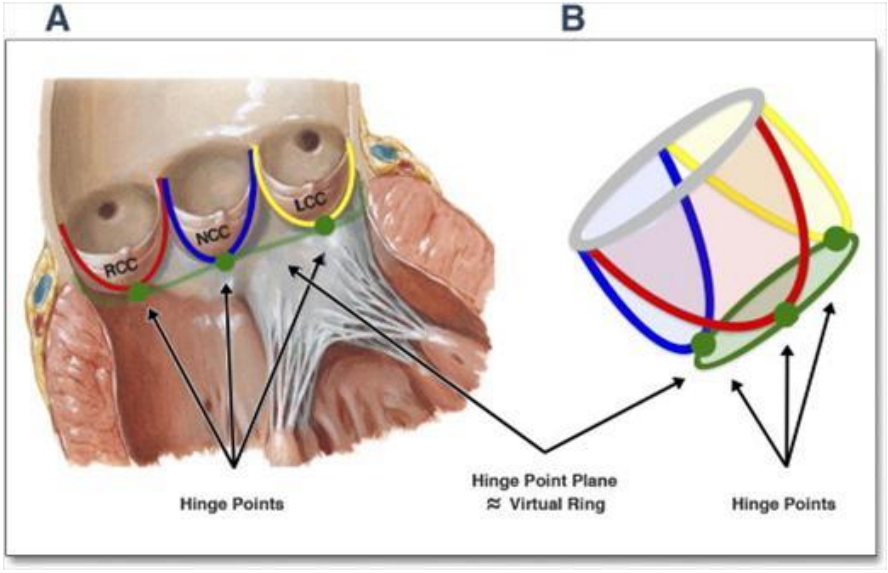

Figure 3. Anatomy of AV leaflet inside a dissected aortic annulus, taken from Kasel [1].

Each leaflet is attached to the aortic annulus base and meets its neighboring leaflet at the sinotubular junction, in a leaflet region called the commissure. The free edge of each leaflet coapts with its neighbor when pressure is applied to the aortic side of the AV. The drop in

LV pressure as diastole begins results in a peak transvalvular pressure of nearly 120mmHg acting on the leaflets' aortic surface.

1.2.2 Aortic Valve Calcification

Valvular heart disease (VHD) is the dysfunction of at least one heart valve and is attributed to 10% to 20% of cardiac surgeries [2]. The American Heart Association reported that in 2013, 67.5% of VHD-related deaths were due to AV disorders [3]. Two common disorders of the AV are calcific aortic stenosis and bicuspid aortic valve disease. Aortic stenosis (AS) is an age-related disease in which narrowing of the AV prevents proper valve closure and opening. Moderate or severe aortic stenosis occurs in 2.8% of patients over the age of 75 [3]. Calcium deposition can lead to severe local thickening which restricts leaflet bending, eventually resulting in valve insufficiency.

Early investigation of calcium deposition patterns revealed a strong correlation between nodule formation and regions of high mechanical stress [4]. In one study, 221 leaflets were examined and 87% of calcified leaflets followed a specific trend [5]. An illustration of two common calcification regions is shown in Figure 4.

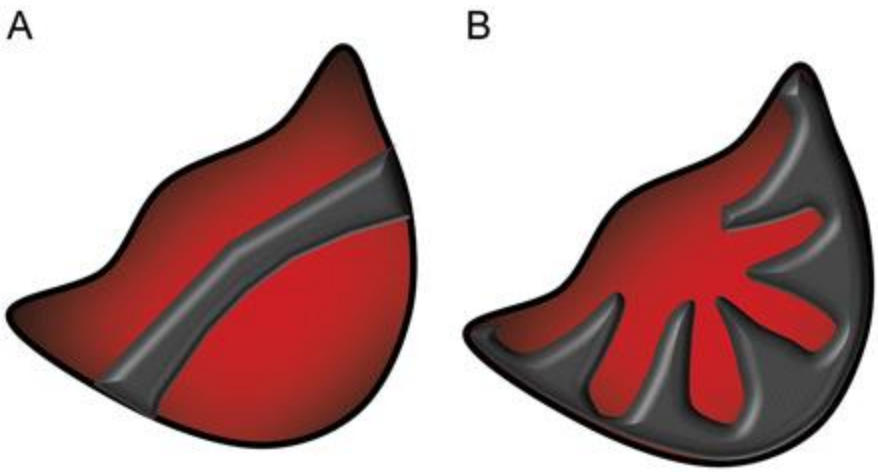

Figure 4. Typical patterns of calcium deposition in native aortic valves commonly develop circumferentially, across the belly (A) or radially, along the attachment edge (B) [6].

The largest degree of flexion occurs at the cusp attachment and secondary bending is observed near the line of coaptation. Therefore, it is believed that mechanical stress induces local tissue degeneration and subsequent calcification initiation.

1.3 Aortic Valve Replacement

Poor performance of the aortic valve, if left unmanaged, can lead to angina, syncope, and dyspnea. Even though aortic valve replacement (AVR) is the preferred treatment for severe AS, a considerable portion of patients do not undergo AVR. In an investigation of nearly 1000 patients across 10 centers, only 41% of patients who met the criteria for severe AS were treated for AVR [7]. Some of the main reasons for not undergoing AVR were comorbidities, high operative risk, and advanced age. The one-year survival rates for patients treated with AVR and unoperated patients were 94% and 69%, respectively.

Aortic valves have been traditionally replaced with a mechanical or bioprosthetic heart valve via open-heart surgery. More recently, however, transcatheter aortic valve

replacement (TAVR) has demonstrated non-inferiority to surgical aortic valve replacement (SAVR) in high-risk populations [8].

1.3.1 Surgical Aortic Valve Replacement

Surgical implantation of prosthetic valves has been considered the gold standard of aortic valve replacement. Surgical pericardial valves, typically composed of chemically-preserved bovine or porcine pericardial leaflets, have stood out for their excellent hemodynamic performance and biocompatibility; however, they are known to have limited durability compared to mechanical valves. Of the currently-available surgical aortic valves, the Carpentier-Edwards Perimount (CEP) valve, shown in Figure 5, is recognized for its long-term durability.

Figure 5. Carpentier-Edwards PERIMOUNT aortic valve bioprosthesis. (courtesy of www.edwards.com)

Despite the CEP valve's expected lifespan of nearly 20 years, surgical aortic valve replacement (SAVR) may not be a suitable option for many patients. As previously mentioned, severe AS typically presents in the elderly population. Advanced age and high operative risk are significant contraindications for open-heart surgery, thus, there is a substantial need for minimally invasive treatment options.

1.3.2 Transcatheter Aortic Valve Replacement

A percutaneous approach to aortic valve replacement was developed for patients considered high-risk for open-heart surgery or completely inoperable. A catheter system is used to insert and position the replacement valve which consists of pericardial leaflets mounted inside of a stent frame. The transcatheter aortic valve (TAV) is deployed using balloon expansion. The first successful transcatheter aortic valve replacement (TAVR) was performed by Cribier in 2002 [9]. Since its introduction, TAVR has been performed in more than 150,000 patients [10].

In the past decade, escalation of surgical proficiency and device modification have helped improve patient outcomes by reducing occurrence of paravalvular leakage, stroke, and vascular injury. Despite TAVRs growing success, it is widely believed that TAV devices suffer from limited durability. A recent computational analysis of bioprosthetic valve fatigue predicted TAV durability may be approximately 7.8 years [11]. Interestingly, new clinical data has reported a significant increase in valve degeneration between 5-7 years post-TAVR [12]. Approximately 50% of TAVs experienced degeneration leading to moderate stenosis or regurgitation within 8 years. Not only are clinical studies beginning to elucidate TAVs' long-term durability, they have already revealed some variability in short and mid-term success. It is believed that unpredictable performance may be strongly influenced by incomplete or erratic stent deployment.

1.4 Transcatheter Aortic Valve Design

Special considerations need to be made for TAVR approach. Surgical aortic valves (SAVs) are sewn onto a stent with flexible posts so commissure peaks are capable of radial deflection; however, TAV leaflets are sewn to rigid stent frames and fixed from displacement. Numerical analysis of bioprosthetic pressurization revealed how stent

properties can significantly affect leaflet stress and potentially influence long-term damage [13].

1.4.1 Design Considerations

Several constraints regarding TAV design must be considered in order to ensure successful outcome. During TAVR, the native aortic valve is accessed via transapical or transfemoral approach. Replacement valves are crimped onto a balloon catheter and loaded inside a crimper. Once it is mounted, the stent is collapsed and leaflets are compressed. For a transfemoral procedure, an opening is made in the femoral artery and a pre-dilation balloon is expanded within the native AV to disrupt loose calcium which may interfere with the stent deployment. However, patients who present with narrow, tortuous vessels may not be well-suited for this surgery. Thus, surgeons may elect for the riskier, trans-apical method, where the TAV device is inserted through an incision in the left ventricular apex. Given these options, it is more advantageous to proceed with a transfemoral approach.

Procedural safety of transfemoral-TAVR is facilitated when the diameter of the delivery system is minimized. One approach to reduce diameter is to decrease the thickness of TAV leaflets. Porcine pericardium has been explored as an alternative leaflet material to the traditional bovine pericardium due to its lower thickness. Even though the mechanical properties of porcine and bovine pericardia have been characterized [14], comparison of their properties is limited due to incompatible fixation procedures and testing protocols. Thus, it is unclear how changes in leaflet material may impact TAV performance and what design features may need reevaluation.

1.4.2 Current Device Generations

Currently available, FDA-approved transcatheter valves include the Edwards SAPIEN 3 and the Medtronic CoreValve. The SAPIEN 3, like its predecessors, utilizes glutaraldehyde-treated bovine pericardium as its source material for leaflet fabrication. The balloon-expandable, cobalt-chromium stent frame is encompassed by a skirt at its base to minimize the risk of paravalvular leakage (PVL). Medtronic's CoreValve, on the other hand, uses a flexible, self-expanding Nitinol stent and porcine pericardial leaflets. CoreValve's elongated stent allows it to be anchored along the ascending aorta and leaflets are situated in a supra-annular position. Several modern TAV designs are illustrated in Figure 6.

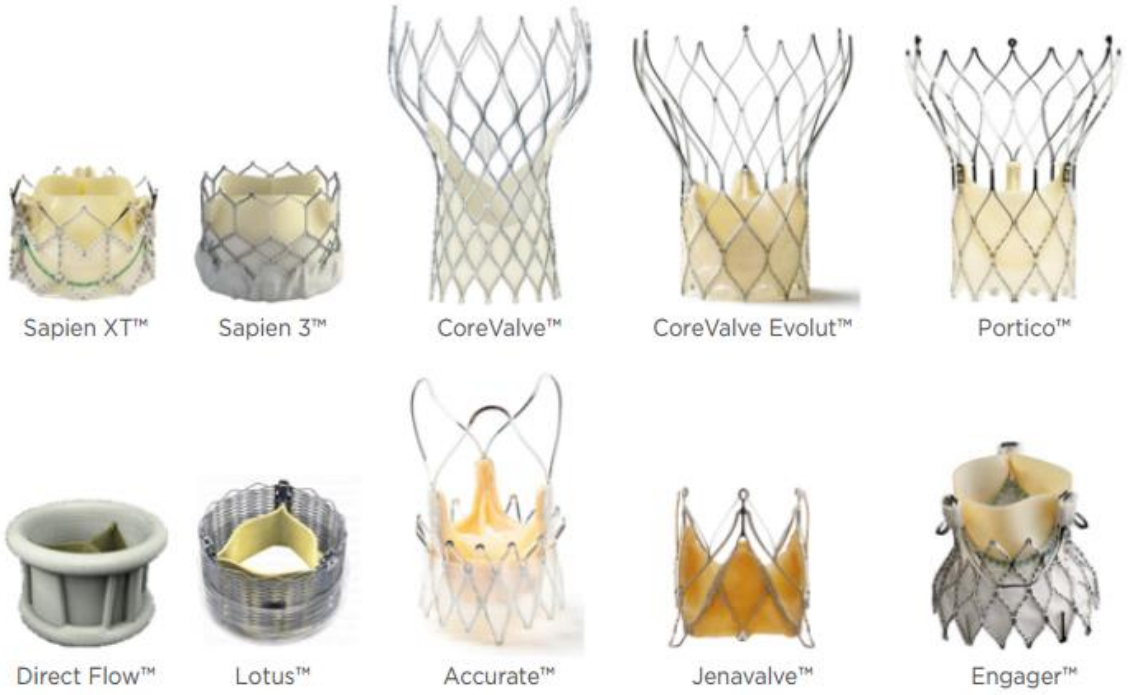

Figure 6. Current generations of TAV designs, adapted from Walther et al. [15].

In addition to the SAPIEN 3 and CoreValve, newer generations of transcatheter valves have emerged and are under investigation. The Lotus valve, for example, features a braided Nitinol stent and bovine pericardium leaflets. The JenaValve uses a special clipping

mechanism to attach its Nitinol frame to the native aortic leaflets, such that the device is actively fixed and less prone to migration. Each TAV device utilizes distinct characteristics; however, leaflet design geometry has remained relatively constant. A representative sequence of transcatheter valves through several design iterations is illustrated in Figure 7.

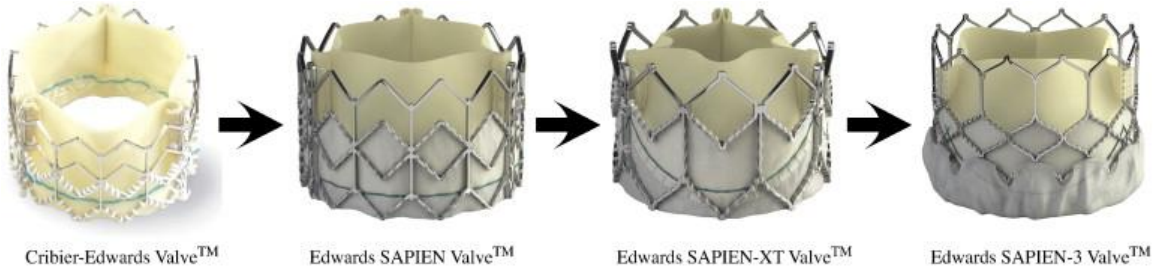

Figure 7. Representative evolution of percutaneous aortic valve design, taken from Fanning et al. [16].

Stent design evolution has improved aspects of device deployment, like valve repositioning and sealing, yet the generic leaflet design adapted from its SAV predecessors has received little attention.

1.4.3 Device Degeneration and Failure

Calcification of bioprosthetic leaflets and cusp tearing are common failure mechanisms of transcatheter valves. Early generations of surgical bioprostheses suffered from deterioration and primary tissue degeneration was reported as the most frequent source of valve failure [4]. Some early generations of valve design, like the Ionescu-Shiley (IS) bioprosthetic surgical valve, suffered from high failure rates and degeneration. Initial examination of IS valves revealed exceptional hemodynamic performance and low incidence of thromboembolism. However, early valve dysfunction became apparent and many patients required reoperation. Surgically removed IS valves often demonstrated

structural disturbance or perforations at the commissure, the former due to calcification and cuspal tears [17]. Similar to the native AV, degenerative calcification predominately occurred in regions of mechanical stress, namely the commissures and attachment edge.

Extensive calcification of native aortic leaflets may constrain the expansion of the transcatheter stent and lead to TAV distortion [18]. TAV misdeployment prevents normal leaflet apposition and increases stress in at least one leaflet [19, 20]. TAV underexpansion due to valve oversizing can also result in significant leaflet distortion [18]. Even though some degree of oversizing can reduce the incidence of PVL [21], patient-prosthesis mismatch may have a significant, deleterious effect on mid-term patient outcomes [22]. It is clear that leaflet mechanics is related to valve deterioration and long-term safety. The relative simplicity of TAV leaflet geometry and significance of mechanical stress lends itself to geometric optimization; however, little information exists on the design of TAV leaflets.

1.5 Design Optimization and Device Safety

Cardiovascular surgery and medical device usage has traditionally taken a trial-and-error approach, where patient outcomes from clinical trials are retrospectively analyzed to determine success. Therefore, there is considerable desire to develop computational tools which can capture the complexity of the geometry and mechanical properties of biological tissue. Numerical simulation of cardiovascular biomechanics could supplement standard clinical imaging and provide more patient-specific information. Enhanced pre-surgical analysis can lead to improved device design and selection. Modern clinical practice has already begun implementing the use of tailored orthopedic devices;

however, patients with cardiovascular disease may suffer from patient-prosthesis mismatch (PPM).

1.5.1 Device Optimization

Classic approaches to design optimization have been applied to investigations of prostheses for knee and hip replacement [23-25]; however, sophisticated numerical analyses of the cardiovascular system and its interaction with implantable devices have only been recently explored [26-29]. The goal of optimization is to identify the best value of an objective while satisfying given requirements. Patient-specific modeling and shape optimization of graft design have been performed in efforts to promote efficient hemodynamics [26, 28, 30]. Although, choosing appropriate objective functions, i.e. performance parameters, can be challenging. Optimizing graft function, for instance, may consist of reducing flow stagnation, maintaining appropriate wall shear stress, decreasing ventricular work, and increasing oxygen delivery. Since long-term durability is a primary concern with transcatheter valve implantation, the cost function for evaluating performance should place emphasis on reducing cyclic stress experienced by valve leaflets.

1.5.2 Robustness and Reliability

Human anatomy can be quite diverse, especially under uncontrollable pathophysiological conditions. Calcium deposition on the native AV may follow general patterns, but the extent of calcification may be varied and asymmetric. The condition of the native leaflets may influence the outcome of stent dilation [31], which can subsequently result in leaflet distortion [18]. Several analyses of TAV eccentricity post-TAVR have demonstrated valve orifice conformation to non-circular shapes [18, 32, 33]. Therefore, it is essential to consider robustness during investigation of TAV leaflet design.

1.6 Project Objective

The objective of this study was to characterize the material properties of pericardial tissue and develop a computational framework to investigate the design of transcatheter aortic valve leaflets. Two specific aims were proposed to achieve this goal.

1.6.1 Specific Aim 1

Quantify the mechanical properties of bovine and porcine pericardium. A structural constitutive model of hyperelastic soft tissue was adopted to describe bovine and porcine pericardia. Material parameters were obtained by curve fitting the model to experimental responses. Data from planar biaxial tension and flexural analysis were integrated into the constitutive models of pericardia. Material properties were implemented into finite element models of TAV leaflets and characteristics of valve opening were investigated.

1.6.2 Specific Aim 2

Develop a computational framework for exploration of TAV leaflet design. The 2D leaflet geometry and 3D attachment edge of TAV leaflets were mathematically parameterized. TAV leaflet models were generated using a virtual assembly method and loaded under diastolic pressure. Influence of design parameters on leaflet stress and inter-leaflet contact were explored using parametric and combinatorial approaches. Geometric optimization of TAV leaflets was performed to reduce maximum principle stress. Nominal and optimal design of bovine pericardial leaflets are examined under elliptical TAV deployment. A robustness-based optimization method is proposed and executed to discover leaflet geometries which demonstrate less variable performance under eccentric TAV expansion.

2 CONSTITUTIVE MODELING OF ANIMAL PERICARDIA

2.1 Collagenous Soft Tissue

Soft collagenous tissues, like blood vessels, skin, and tendons, are biological materials which provide support to other structures in the body. Soft tissues often exhibit complex material characteristics arising from its intricate composition. Medical devices which utilize biological tissue, like cardiovascular grafts, can more easily replicate the behavior of healthy tissues than synthetic materials. Thus, it is of great interest to study the mechanical properties of soft tissue and develop modeling tools which can predict its response to variable conditions.

2.1.1 Structure and Function

The structure and mechanical function of soft tissue are strongly related. The extracellular matrix (ECM) of soft tissue is mainly composed of glycosaminoglycans, elastin bundles, wavy collagen fibers, and water. The ECM plays several important roles: it provides tissue with mechanical strength so that it can maintain its shape; it provides an aqueous environment for diffusion of nutrients; and serves as a bioactive scaffold for cellular attachment, migration, and proliferation. Mechanical integrity of soft tissue is derived from its strong collagen fibers. In an un-loaded condition, collagen fibrils exist in a crimped state with various degrees of periodicity. Collagen fiber straighten out as tissue is mechanically loaded, as illustrated in Figure 8.

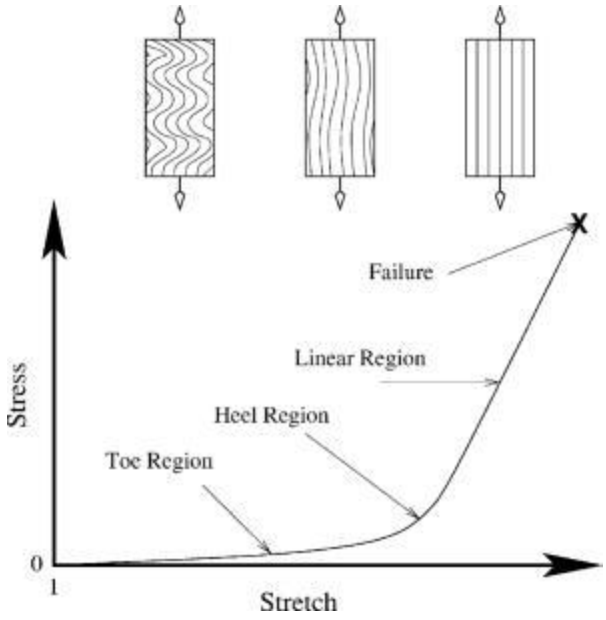

Figure 8. Soft tissue stress-strain response is associated with collagen fiber deformation [34].

The stress-strain relationship of soft tissue usually follows a J-shaped curve. Under low-loading conditions, fibers have freedom to unwrinkle and slightly rotate, as a result, the non-collagenous components of the ECM dominate the mechanical response under low tissue strain. Once fibers are uncurled, load-bearing responsibility transitions to collagen and the tissue response stiffens considerably. By understanding how tissue architecture influences mechanical function, sophisticated constitutive models may be developed to more accurately reflect soft tissue behavior.

2.1.2 Mechanical Characterization of Soft Tissue

Planar biaxial testing has been used to capture the anisotropic properties of many soft tissues, including skin, blood vessels, and tendons. In order to obtain the stress-strain relationship from biaxial testing data, it is first necessary to understand basic mechanics related to continuous bodies.

Consider a generic mapping between a body's undeformed, i.e. reference state, and a deformed configuration. Displacement of each point can be described by its current, $\boldsymbol{x}$, and original, $\boldsymbol{X}$, position.

$$\boldsymbol{u}(\boldsymbol{X}, t) = \boldsymbol{x}(\boldsymbol{X}, t) - \boldsymbol{X} \quad (1)$$

The deformation gradient, $\boldsymbol{F}$, is a second-order tensor which maps the physical transformation.

$$\boldsymbol{F} = \frac{\partial \boldsymbol{x}}{\partial \boldsymbol{X}} = \begin{bmatrix} \frac{\partial x_1}{\partial X_1} & \frac{\partial x_1}{\partial X_2} & \frac{\partial x_1}{\partial X_3} \\ \frac{\partial x_2}{\partial X_1} & \frac{\partial x_2}{\partial X_2} & \frac{\partial x_2}{\partial X_3} \\ \frac{\partial x_3}{\partial X_1} & \frac{\partial x_3}{\partial X_2} & \frac{\partial x_3}{\partial X_3} \end{bmatrix} \quad (2)$$

$\boldsymbol{F}$ is a fundamental measure of deformation from which important metrics like strain, strain rate, and volume change can be derived. Soft tissues are generally considered incompressible materials due to their high water content, thus

$$J = \det(\boldsymbol{F}) = 1 \quad (3)$$

Even though $\boldsymbol{F}$ is a fundamental measure of deformation, it is generally not symmetric and may not be the most convenient metric for elasticity analysis. A more appropriate descriptor, the right Cauchy-Green tensor, is defined as

$$\boldsymbol{C} = \boldsymbol{F}^T \cdot \boldsymbol{F} \quad (4)$$

In turn, the most common form of strain, the Green-Lagrange strain tensor can be written as

$$\boldsymbol{E} = \frac{1}{2}(\boldsymbol{C} - \boldsymbol{I}) \quad (5)$$

where $\boldsymbol{I}$ is a second order identity tensor. Experimentally, $\boldsymbol{F}$ is determined by tracking optical markers and calculating displacements. An image of the planar biaxial testing system setup and representative tissue mounted onto the machine is shown in Figure 9.

Several definitions of stress tensors have also been proposed. The Kirchhoff stress tensor, for example, is defined as the product of Cauchy stress, $\boldsymbol{\sigma}$, and the Jacobian of the deformation gradient tensor:

$$\boldsymbol{\tau} = J\boldsymbol{\sigma} \tag{6}$$

However, the second Piola-Kirchhoff stress tensor, **S**, a symmetric tensor defined in material coordinates is obtained via pull-back operation of $\boldsymbol{\tau}$.

$$\boldsymbol{S} = \boldsymbol{F}^{-1}\boldsymbol{\tau}\boldsymbol{F}^{-T} \tag{7}$$

While **S** has no real physical interpretation, it is convenient to use this stress definition in the formulation of constitutive models of solid materials.

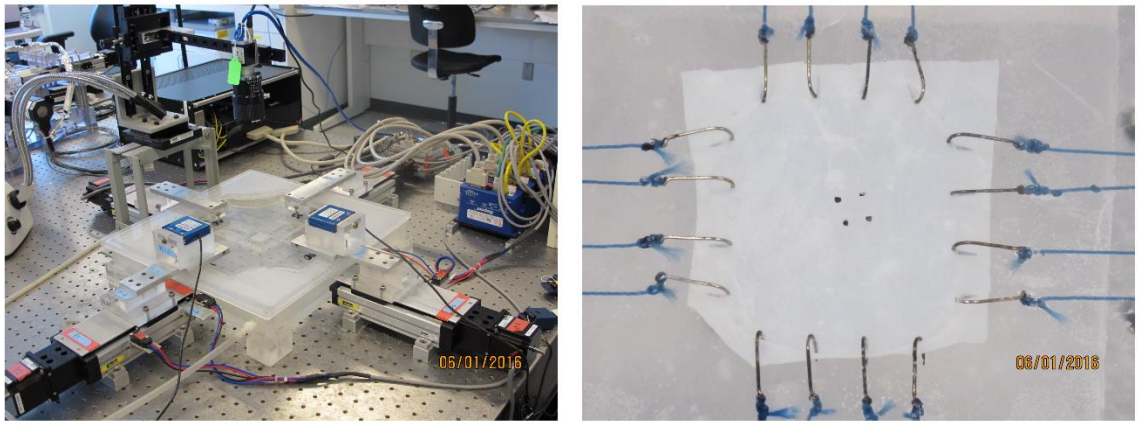

Figure 9. Biaxial setup (left), where tissue is loaded using sutures (right).

2.1.3 Modeling Soft Tissue Mechanics

Biological soft tissue is a highly anisotropic material which undergoes large deformations and exhibits nonlinear stress-strain relationships. As a result, sophisticated material models are required to adequately describe soft tissue behavior. Since collagenous

soft tissue acts like a hyperelastic material, the stress response can be derived using a strain energy function, W. Specifically, the Second Piola-Kirchoff stress tensor, $\boldsymbol{S}$, is expressed by

$$\boldsymbol{S} = \frac{\partial W}{\partial \boldsymbol{E}} \tag{8}$$

Many forms of the strain energy density function have been proposed. Ogden used principal stretches, λ_i, to describe the strain energy of incompressible, isotropic materials.

$$W = \sum_{p=1}^{N} \frac{\mu_p}{\alpha_p} (\lambda_1^{\alpha_p} + \lambda_2^{\alpha_p} + \lambda_3^{\alpha_p} - 3) \tag{9}$$

where μ_p and α_p are material constants. The Ogden model is commonly used to model rubber-like materials; however, an anisotropic model is required to accurately capture the soft tissue response.

The Mooney-Rivlin model of strain energy was used to express W in terms of the first and second strain invariants. A generic description of an incompressible Mooney-Rivlin material is given by

$$W = c_1(\bar{I_1} - 3) + c_2(\bar{I_2} - 3) \tag{10}$$

where c_1 and c_2 are material constants and I_1 and I_2 are the first and second invariants of $\boldsymbol{C}$, defined as

$$\bar{I_1} = tr(\boldsymbol{C}) \tag{11}$$

$$\bar{I_2} = \frac{1}{2}[\big(tr(\boldsymbol{C})\big)^2 - tr(\boldsymbol{C}^2)] \tag{12}$$

The classic neo-Hookean model can be obtained from Equation 10 by setting c_2 to zero. The Mooney-Rivlin model may be appropriate for nearly isotropic materials; however, its

inability to capture the stiffening effect in large strain domains limits its application to biological materials [35].

A hyperelastic material model proposed by Fung [36] has been widely used to characterize the mechanical behavior of soft tissue. A generalized Fung-type constitutive model, based on Green strain, can be written as

$$W = \frac{c}{2}(e^{Q} - 1) \tag{13}$$

$$Q = A_1 E_{11}^2 + A_2 E_{22}^2 + 2A_3 E_{11} E_{22} + A_4 E_{12}^2 + 2A_5 E_{11} E_{12} + 2A_6 E_{22} E_{12}$$

where c and A_i are material constants. Equation 13 has been used to model the anisotropic properties of soft tissue using planar biaxial testing [37]. The Fung model has been extensively implemented to plane stress elements in finite element analyses of thin soft tissues [37]. One shortcoming of this approach is the absence of transverse shear stiffness. Without definition of transmural behavior, the transverse shear stiffness must be assumed. Previous finite element modeling of bioprosthetic valve loading revealed that diastolic pressurization was insensitive to transverse shear stiffness [38]. Despite its success in simulating bioprosthetic heart valve deformation, the Fung model formulation is phenomenological in nature. Thus, it not possible to ascribe relationships between tissue structure and mechanical function.

A novel, invariant-based structural constitutive framework was proposed by Holzapfel [39]. The Holzapfel model, inspired by the passive mechanical response of biological soft tissue, describes the behavior of fiber-reinforced materials. The strain energy function is considered a composition of isotropic, anisotropic, and volumetric constituents.

$$W = W_{iso} + W_{aniso} + W_{vol} \tag{14}$$

Where the isotropic and anisotropic deformations components represent the non-collagenous ground substance and collagen fibers, respectively. In addition to the strain invariants given by Equations 11 and 12, the properties related to fiber families are given by

$$\overline{I_{4i}} = \boldsymbol{m}_{0_i} \cdot \boldsymbol{C}\boldsymbol{m}_{0_i} \tag{15}$$

where i indicates the fiber family whose preferred direction is given by $\boldsymbol{m}_0 \otimes \boldsymbol{m}_0$. Specific forms of Equation 14, have been expressed by

$$W_{iso} = C_{10}(\overline{I_1} - 3) \tag{16}$$

$$W_{aniso} = \frac{k_1}{2k_2} \sum_{i=4,6} [\exp\{k_2[\kappa \overline{I_1} + (1 - 3\kappa)\overline{I_{4i}} - 1]^2\} - 1] \tag{17}$$

where C_{10}, k_1, and k_2 are material parameters [40]. Obviously, the isotropic contribution is described using a neo-Hookean model. An exponential function is employed in the description of strain energy for collagen fibers so that the stiffening effect observed at high strain may be captured. The parameter κ represents the dispersion of embedded collagen fibers. A material with ideal fiber alignment is symbolized by the lower limit, i.e. κ approaches 0. In contrast, the upper limit, i.e. $\kappa = 1/3$, describes a perfectly isotropic distribution of collagen fibers.

2.2 Experimental Testing and Modeling

The mechanical properties of bovine and porcine pericardium were determined experimentally using planar biaxial tension and cantilever bending. Here, traditional beam bending is performed using bovine and porcine pericardial tissues of multiple thickness groups. Biaxial testing data of bovine and porcine pericardia are fit to a structural constitutive model and material parameters are obtained. Inverse finite element analysis

(FEA) of tissue bending is performed and material constants are optimized. Material parameters derived from both flexural and biaxial testing are implemented in FEA simulations of valve opening under physiological loading conditions and compared.

2.2.1 Material Preparation

Bovine and porcine pericardia were collected after slaughter (Animal Technologies, Tyler, TX) and stored on ice before preparation. Fatty nodules were removed cautiously and large sections were pinned in a trampoline fashion without overextension. Fresh BP and PP sheets were treated with 0.625% glutaraldehyde (GL) solution for 18 hours, then placed in crosslinking solution (6% Formaldehyde, 2.2% Ethanol, 1.2% Tween 80) for 2 hours before final transfer to 0.25% GL solution at 4° C. Tissue selection was performed by examination of thickness homogeneity in flat regions of pericardial sheets. Rectangular segments of BP (12 x 5.75 mm) and PP (7.5 x 6.5 mm) tissue were cut in uniform dimensions for cantilever bending tests. Tissue thickness was measured in three areas along the length of the sample using a non-rotating thickness gauge (Mitutoyo, Model 7301) and the mean value was documented. For biaxial testing, tissue was selected based on thickness uniformity and homogeneity of fiber distribution; samples were cut into square pieces (20mm x 20mm) of pericardium.

2.2.2 Biaxial Testing

Four graphite markers were attached to one side of the tissue specimen using a small amount of adhesive. Tissue samples were mounted in a trampoline manner by running continuous lines of suture along each edge and submerged in 0.9% NaCl solution maintained at 37° C. Fish hooks were used to access a 2cm x 2cm square region in the center of each tissue sample. 30 preconditioning cycles were performed to diminish the

effect of hysteresis and provide a stable mechanical response. A stress-controlled protocol in which the ratio of Lagrangian stress components, T_{11}:T_{22} was employed where $T_{12} = T_{21} = 0$. Seven experimental protocols were performed in which T_{11}:T_{22} = 1:1, 0.75:1, 0.5:1, 0.3:1, 1:0.75, 1:0.5, and 1:0.3.

2.2.3 Cantilever Bending

A cantilever beam setup was established by pinning each tissue strip on one end and allowing the rest of the specimen to free float in water. A small needle with suture was fed through the free end of the tissue such that the weight of the needle pulled the tissue beam downward. A ruler was fixed in place near the beam for calibration during subsequent image analysis. Two individual weights were applied to BP (125, 56mg) and PP (45, 19mg) segments. Image digitization was carried out using custom Matlab (MathWorks Inc., Natick, MA) scripts. Images were individually cropped and converted to binary using a background-level threshold. Two horizontal points along the calibration ruler were used to determine the pixel-to-mm ratio. After digitization, points along the deflection curve were fit to a third-order polynomial. Vertical coordinates along the length of the beam were averaged between specimens to obtain a mean flexure response.

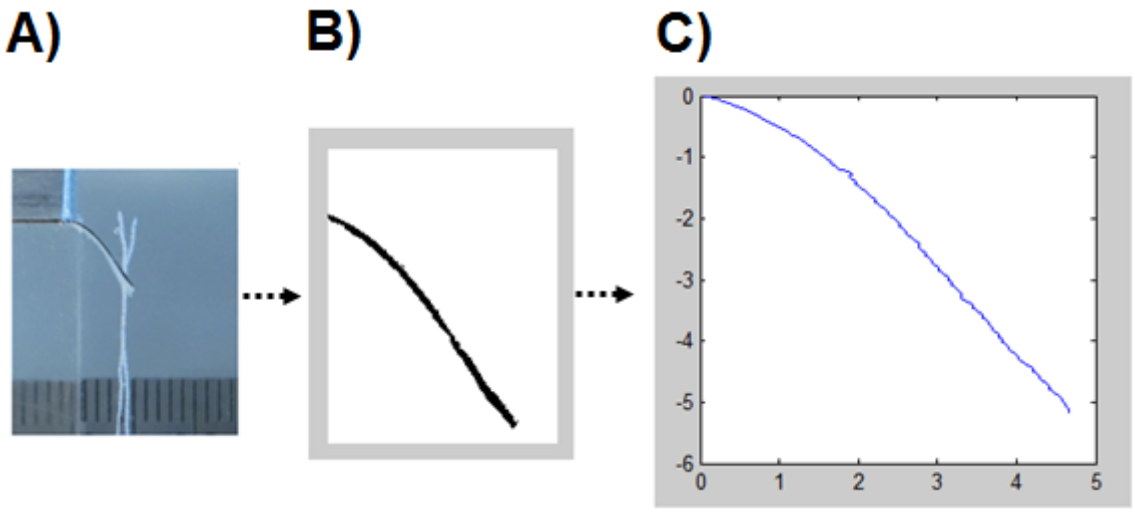

Figure 10. Representative sequence of image acquisition (A), thresholding (B), and digitization (C).

A representative example of the digitization process is presented in Figure 10.

2.2.4 Inverse FEA

The 3D tissue geometries were created using average dimensions of BP and PP specimens. Commercial software for finite element analysis (FEA), Abaqus\Standard 6.13 and process automation, Isight 5.9 (Dassault Systemes Simulia Corp, Johnston, RI), was used to implement inverse FEA. Cantilever bending was performed by fixing the nodes along one end of the tissue from displacement and applying a concentrated force to the free end. Bovine and porcine pericardia are assumed to be anisotropic, incompressible, nonlinear, hyperelastic materials. The strain energy function was defined using a fiber-reinforced, hyperelastic material model inspired by traditional structural modeling.

$$W = C_{10}\{\exp[C_{01}(\bar{I}_1 - 3)] - 1\} + \frac{k_1}{2k_2}\sum_{i=1}^{2}\{\exp[k_2(\bar{I}_{4i} - 1)^2] - 1\} + \frac{1}{D}(J-1)^2 \quad 18$$

Where C_{10}, C_{01}, k_1, k_2, and D are material constants; $\bar{I}_1$ and $\bar{I}_{4i}$ are deviatoric strain invariants. Parameters C_{10} and C_{01} characterize the matrix material, while k_1 and k_2

represent the response of collagen fibers. Material constant D controls incompressibility and J is the determinant of the deformation gradient tensor. Least-squares curve fitting was performed on stress-strain data from recent biaxial testing of bovine and porcine pericardium. The material constants obtained from curve fitting were implemented in a user-defined material (UMAT) subroutine in Abaqus. Python scripts were used to extract node coordinates from the deformed configuration at timesteps corresponding to each loading state. Computational deformation was fit to the mean experimental response by specifying the polynomial coefficients and the resulting coefficient of determination (R^2) was recorded.

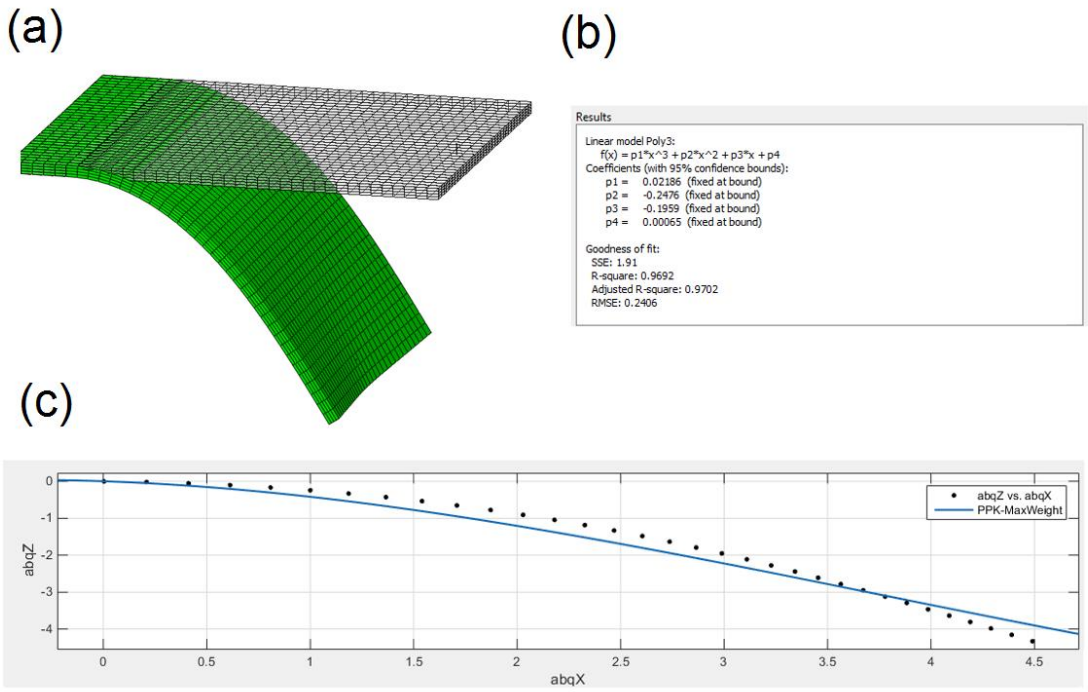

Figure 11. FEA bending (a) compared to experimental fit parameters (b). Side-by-side comparison of deflection curves (c).

Comparison of experimental and computational deflection curves is demonstrated in Figure 11. The coefficient of determination for the larger weight, i.e. 125mg and 56mg,

was denoted as R_1^2, while the coefficient of determination of the lower weight, i.e. 45mg and 19mg, were denoted as R_2^2.

2.2.5 FEA Flexure Optimization Framework

The optimization component within Isight was chosen for its selection of multi-objective search techniques. The Archive-based Micro Genetic Algorithm (AMGA) was selected to explore the parameter space. The coefficient of determination from both loading conditions, R_1^2 and R_2^2, were set as the objective functions with equal weights. An illustration of the Isight workflow is presented in Figure 12.

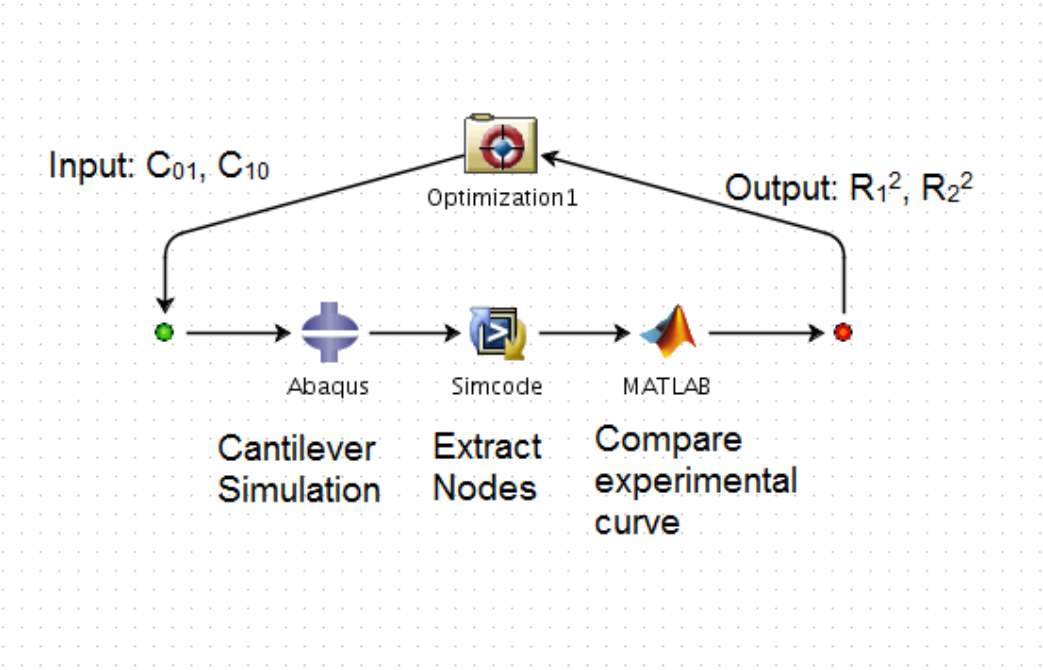

Figure 12. Optimization scheme for identifying appropriate material parameters.

After searching the parameter space, least-squares curve fitting was again performed on biaxial data for each tissue group using Equation 18. Non-matrix related terms, i.e. k_1 and k_2, were fixed at their original values and matrix-related parameters C_{01} and C_{10} were constrained to their optimal ranges.

2.2.6 Valve Modeling

A previously described FE model of a generic, 23 mm TAV was used in this study [41]. The undeformed shell model was imported into HyperMesh 12.0 (Altair Engineering, Troy, MI) and a bi-layer, solid element model was generated; each leaflet was discretized into 5394 large-strain brick (C3D8) elements. The average thickness of BP and PP leaflets reported from experimental testing were used for each group. The mechanical properties defined by Equation 18 were implemented into Abaqus using a user subroutine UMAT. Deformation of the TAV stent was assumed to be negligible; therefore, stent geometry was excluded from the analysis. Nodes along the stent-attachment line were fixed from displacement to mimic attachment to a rigid stent.

In-house Python scripts were used to export images of valve deformation taken from the x-y plane and calculate the geometric orifice area (GOA) at each time step. Key stages in the data acquisition process are demonstrated in Figure 13.

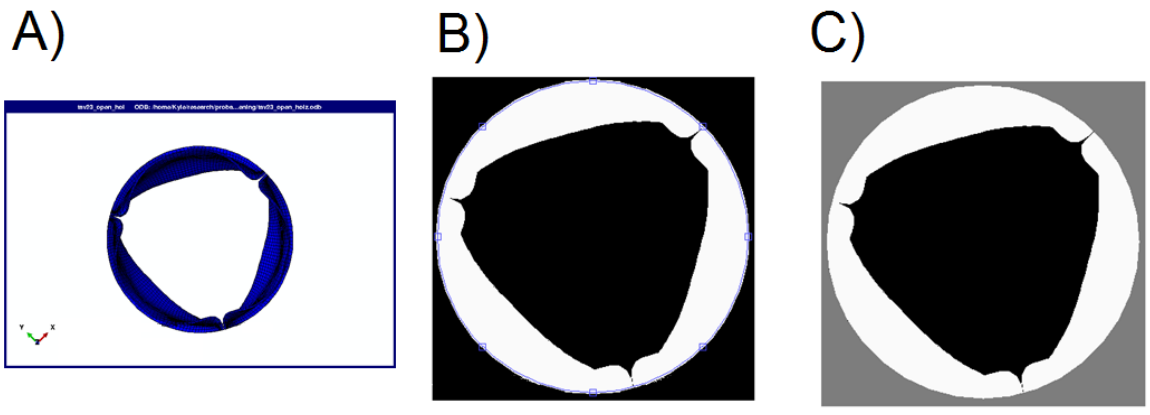

Figure 13. Planar images are extracted from Abaqus (A), converted to binary (B), and GOA is calculated (C).

Images were imported into Matlab and converted to binary using an appropriate threshold. Since nodes along the outside of the valve orifice were fixed, a circular region of interest was used to remove background pixels (gray region, Figure 13) and determine the pixel-

to-length ratio. Black and white pixels were totaled and the ratio was used to calculate the geometric orifice area. In this way, GOA was computed in a manner similar to aortic valve planimetry, a clinical method used to measure aortic valve area.

2.3 Pericardium Flexure and TAV Modeling

The thickness of thick BP (BPK, 0.45 ± 0.03 mm), thin BP (BPN, 0.32 ± 0.03 mm), thick PP (PPK, 0.20 ± 0.03 mm), and thin PP (PPN, 0.14 ± 0.02 mm) tissues were recorded.

2.3.1 Biaxial Testing

Glutaraldehyde-treated bovine and porcine pericardia exhibited nonlinear, anisotropic constitutive relationships. Average experimental responses obtained from biaxial testing for each of the seven testing protocols are shown in Figure 47-Figure 50 in Appendix A. A representative fitting of an averaged stress-strain response is presented in Figure 14.

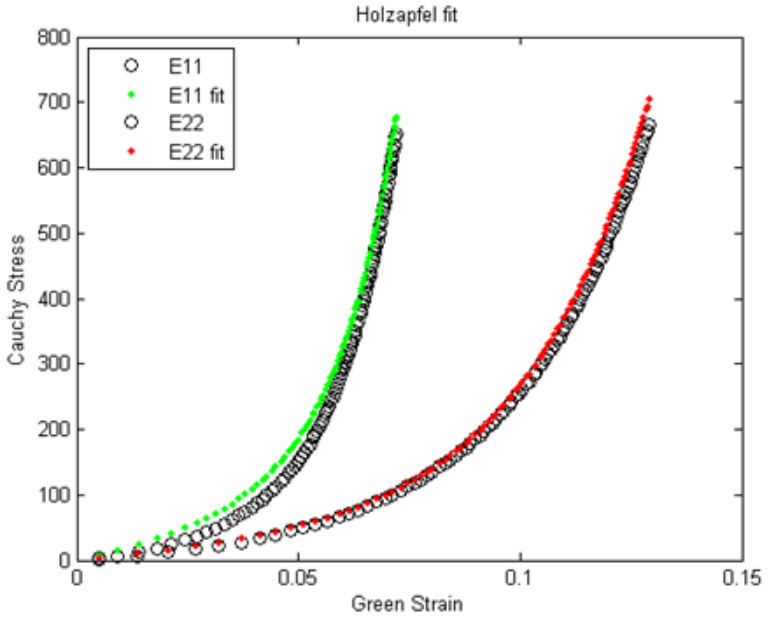

Figure 14. Constitutive model fitting of average PPK deformation (only 1:1 loading protocol shown), where 11 and 22 are the preferred- and cross-fiber directions, respectively.

Material model parameters obtained from constitutive curve fitting are listed in Table 1.

Table 1. Material model parameters from curve fitting mean biaxial responses.

	C_{01}	k_1 (kPa)	k_2	C_{10} (kPa)	κ	Θ (°)	R^2
BPK	11.163	10.37191	37.1714	8.385	$3.7e^{-11}$	0.016	0.9677
BPN	13.222	27.8908	56.3524	4.814	$9.98e^{-3}$	8.32	0.9614
PPK	26.486	109.6696	91.9787	2.866	$2.05e^{-9}$	0.002	0.9788
PPN	32.111	152.6404	107.272	2.044	$1.16e^{-7}$	7.81	0.9872

As demonstrated by the consistently low κ and θ values, collagen fibers were strongly aligned with a particular loading axis. The modified-Holzapfel model was able to capture the stress-strain relationship of each material very well, as evident by the high coefficients of determination reported in Table 1. Generally, porcine tissues exhibited a stiffer response than bovine in both the preferred- (X1) and cross-fiber (X2) directions.

2.3.2 Flexural Testing

The average deflection curve for each tissue group is shown in Figure 15.

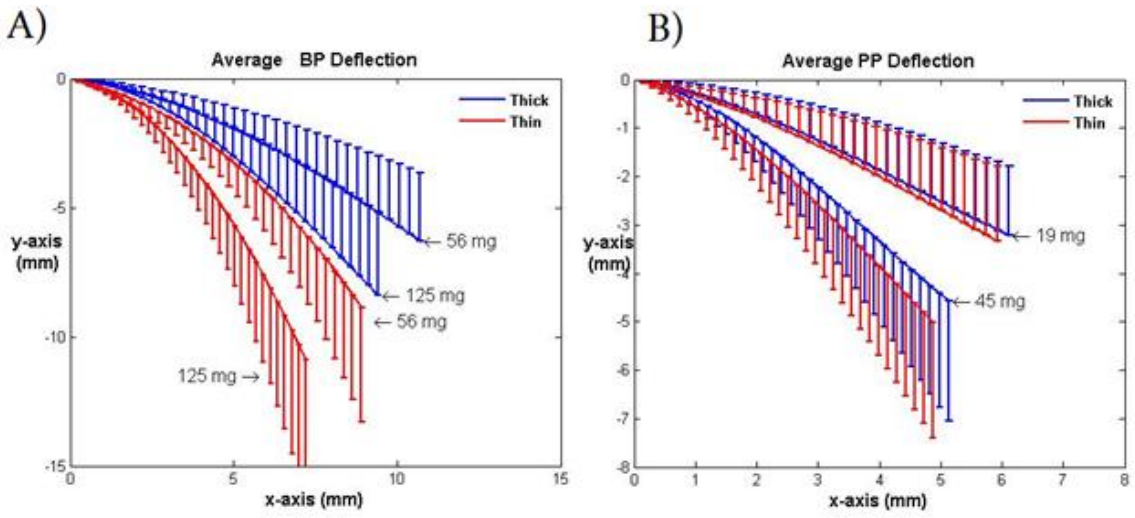

Figure 15. Average deflection curves for bovine (A) and porcine (B) tissues.

On average, bending of thin tissues produced greater deflection than their thicker counterparts and this difference was most notable for bovine pericardium.

2.3.3 Inverse FEA

Finite element simulations were able to accurately model the experimental bending response. In Figure 16 and Figure 17, simulated deflection using material constants obtained from biaxial curve fitting and the optimized parameters are compared to experimental bending.

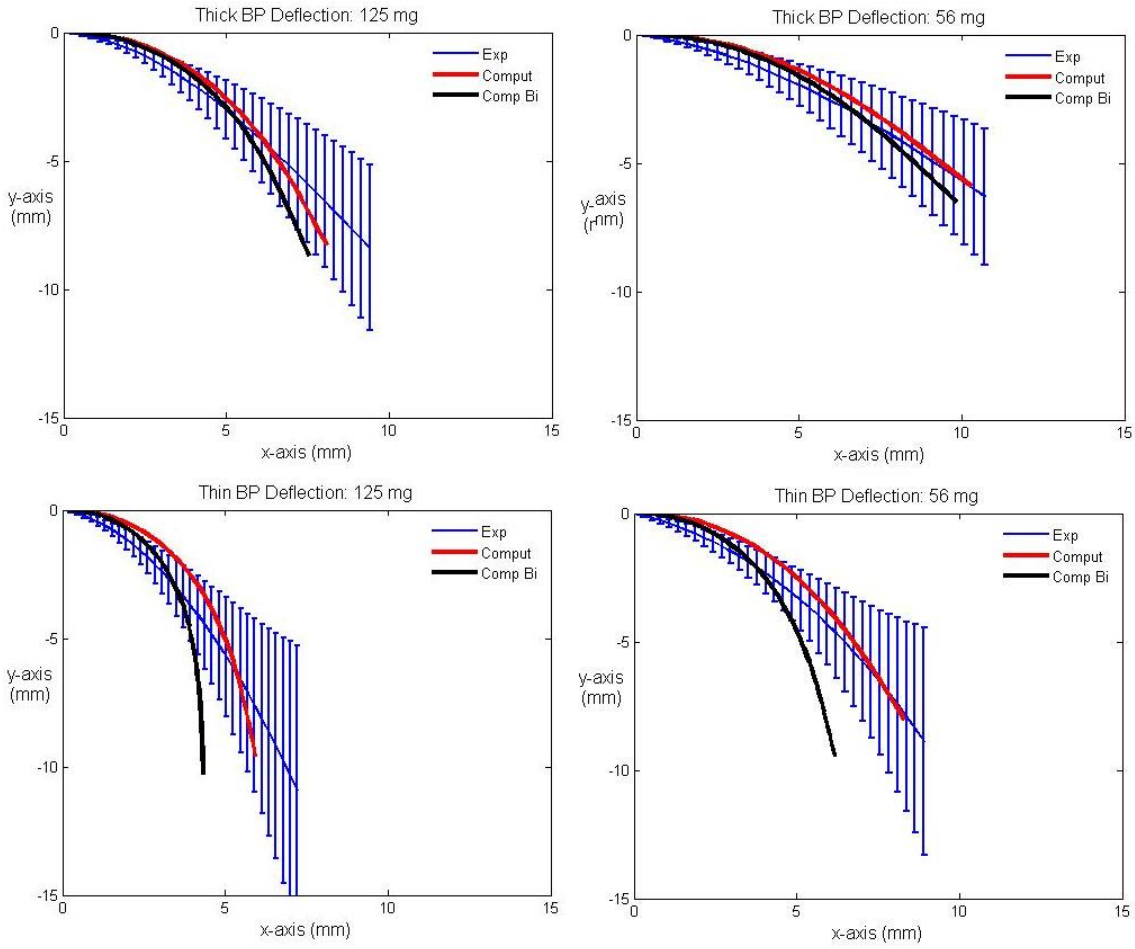

Figure 16. Average experimental deflection curves (blue) compared to FEA deflection resulting from the original biaxial parameters (black) and bending-optimized parameters (red). 125 mg (left) and 56 mg (right) weights were used for thick (top) and thin (bottom) bovine pericardium.

In all conditions, the optimized material constants provided a more accurate deformation than the biaxial-derived parameters.

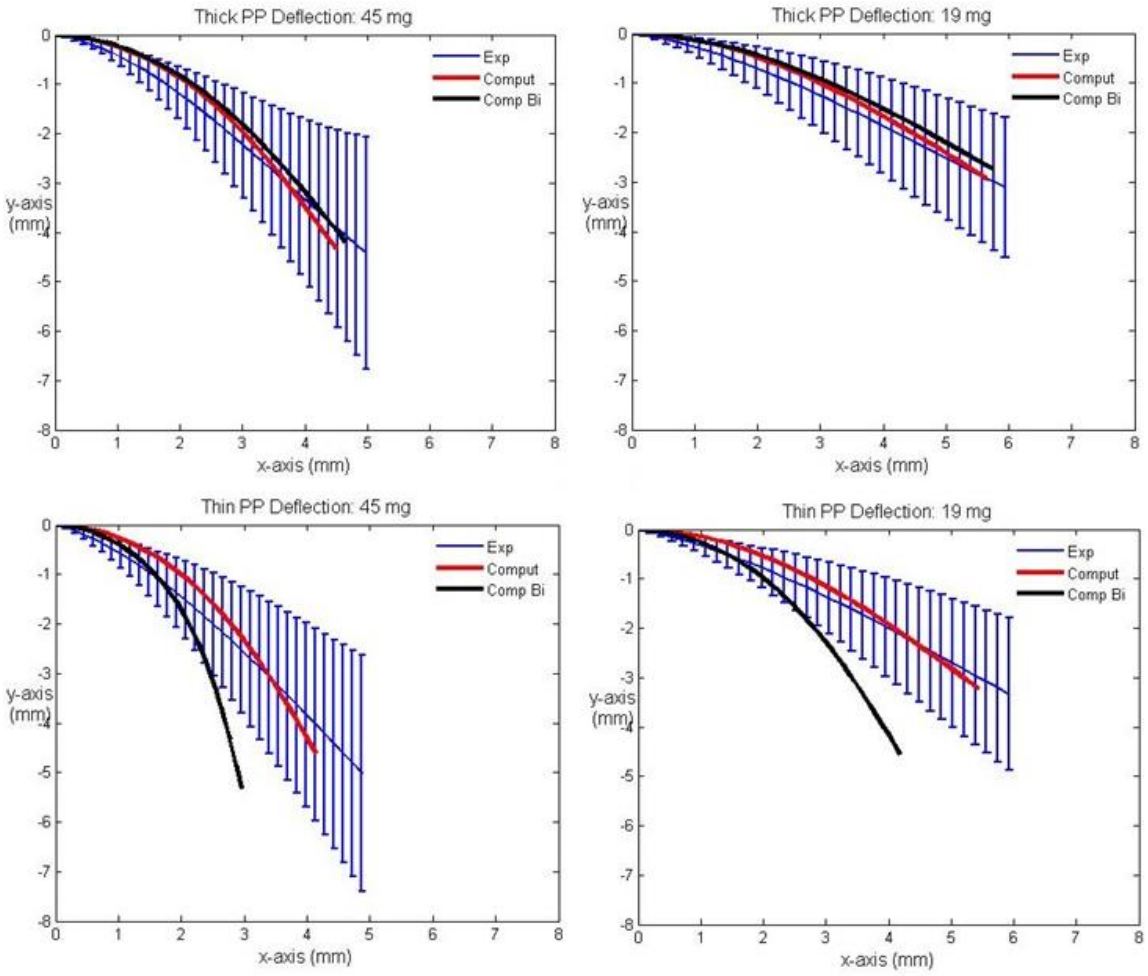

Figure 17. Average experimental deflection curves (blue) compared to FEA deflection resulting from the original biaxial parameters (black) and bending-optimized parameters (red). 45mg (left) and 19mg (right) weights were used for thick (top) and thin (bottom) porcine pericardium.

Material model coefficients obtained from a biaxial-only approach tended to produce a softer flexural response in nearly all tissue deflections. Corrections to C_{01} and C_{10}, the parameters governing the low-strain, isotropic response, resulted in deflections that were more accurate in regards to tip deflection magnitude and beam shape.

Absolute values of C_{01} and C_{10} were not strongly correlated with deflection accuracy; however the product of the two parameters, denoted as CC, determined the goodness of fit. The effect of CC on the averaged fitting is demonstrated in Figure 18.

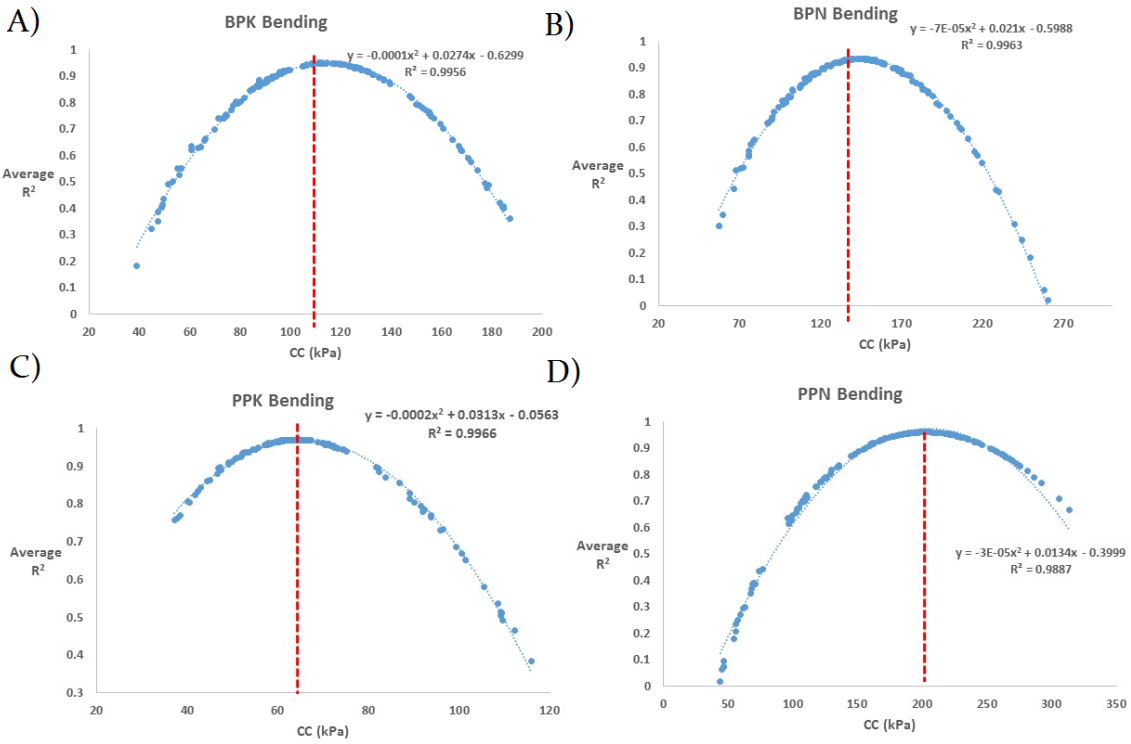

Figure 18. Influence of *CC* on the average coefficient of determination.

The relationships between *CC* and the objective function were well characterized by second order polynomials. The value of *CC* at the maximum R^2 is reported for each material in Table 2. Biaxial data was successfully re-fit after implementing constraints for C_{10} and C_{01}, the resulting parameters are recorded in Table 2.

Table 2. Material parameters obtained after bending optimization and biaxial re-fitting.

	C_{01}	k_1 (kPa)	k_2	C_{10} (kPa)	CC (kPa)	R^2
BPK	9.8502	10.37191	37.1714	11.6045	114.3	0.9658
BPN	7.9345	27.8908	56.3524	18.5987	147.6	0.9339
PPK	28.5449	109.6696	91.9787	2.3196	66.21	0.9781
PPN	13.4848	152.6404	107.272	15.1414	204.2	0.9252

Bending-adjusted material coefficients were generally less compliant than their biaxial-derived counterparts, most notably for BPN and PPN tissues. The difference between matrix constants was apparent when material models were applied to valve opening

simulations. The position of nodes along the leaflet midline was extracted from the undeformed and deformed valve configurations. Juxtaposition of midline points, as seen in Figure 19, highlights the increased deformability of porcine samples compared to bovine tissue.

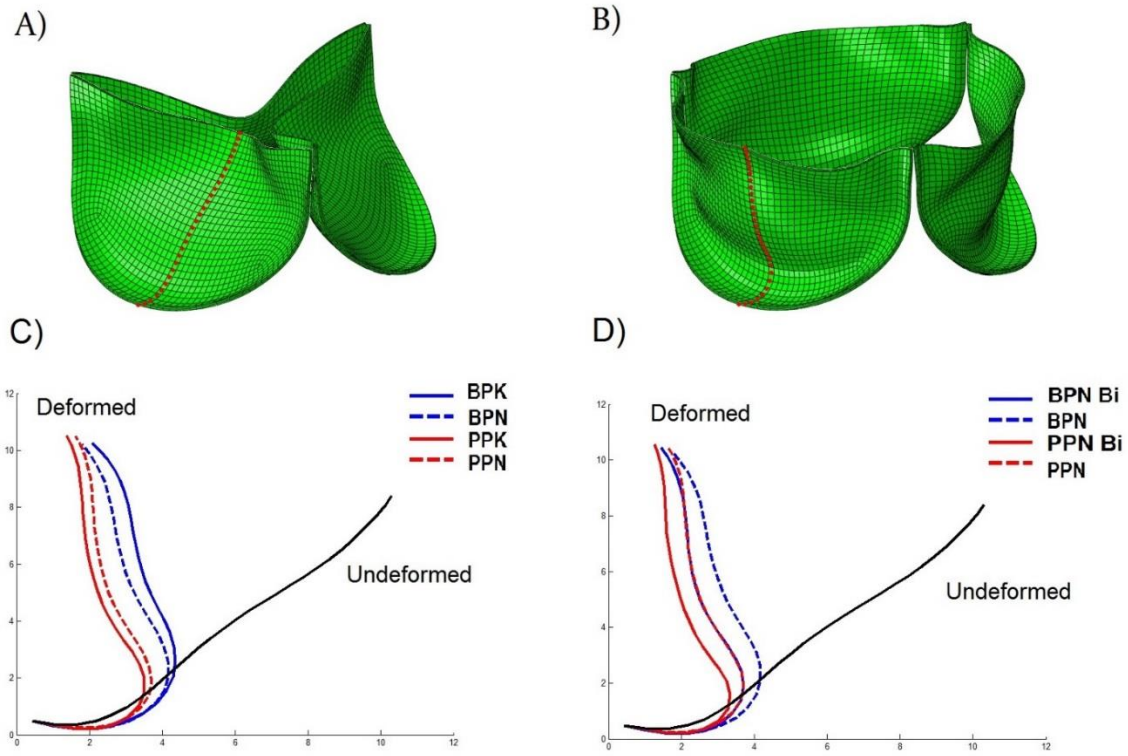

Figure 19. Comparison of undeformed (A) and deformed (B) valve deformation with leaflet midline nodes highlighted in red. Midline deflection curves (C, D) after systolic pressurization, Δp = 4mmHg. Comparison of leaflet models using biaxial and flexure-derived parameters (C). Evaluation of select models with parameters derived from biaxial-only data (solid lines) and biaxial-flexure data (dashed lines).

In the cases of BPN and PPN, material model adjustment resulted in a substantial reduction of flexibility. The increased stiffness of these two groups was similarly indicated by the decrease in valve GOA, illustrated in Figure 20.

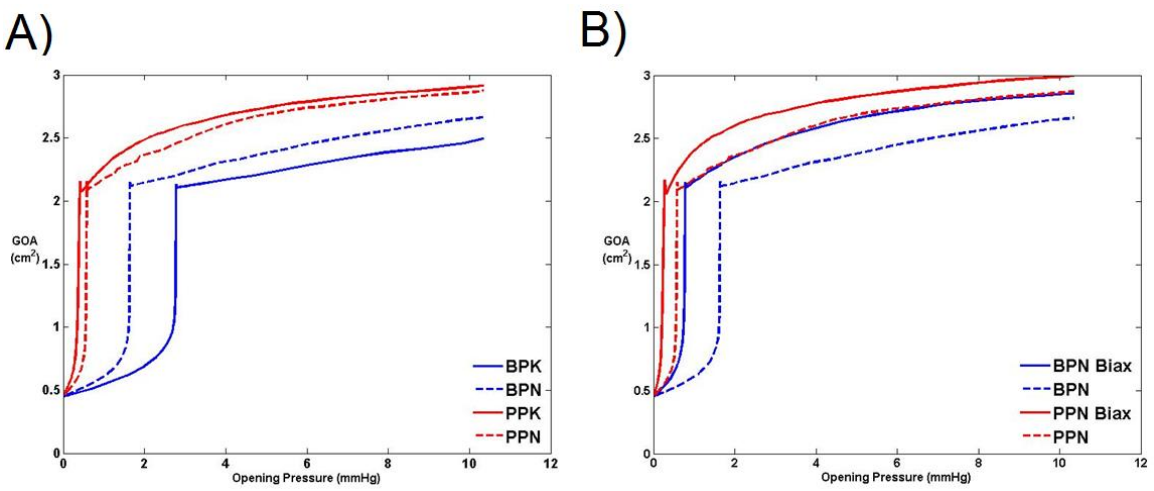

Figure 20. Relationship between GOA and pressure for all four tissue groups (A). Comparison of material coefficients for thin groups (B)

Valve deformation developed comparably between tissue types during opening. Leaflets opened rapidly after reaching threshold pressure, then plateaued. Threshold pressures were 2.77, 1.64, 0.38, and 0.57 mmHg for BPK, BPN, PPK, and PPN tissues, respectively. The extent of valve area converged for each group, yet the porcine leaflets exhibited greater flexure than bovine. While both porcine valves reached GOAs approaching 3cm^2, BPN plateaued around 2.6cm^2 and BPK stayed below 2.5 cm^2. As with midline deflection, parameters derived from bending demonstrated a stiffer response than those fit using biaxial curve fitting. When comparing GOA at a pressure gradient near 4mmHg, relative difference between material models were 10.9% and 6.4% for BPN and PPN, respectively. Material parameters which accounted for flexural deformation consistently predicted a smaller orifice area than models which implemented material coefficients exclusively derived from biaxial testing data.

2.4 Discussion

In the current study, data from cantilever bending and biaxial tensile testing were assimilated into constitutive law. Comparison of TAV opening simulations revealed substantial differences between tissue types and mechanical testing methodologies. In this work, inverse FEA and structural constitutive modeling were employed to approximate the material response to flexural loading. This is in contrast to previous work in which Euler-Bernoulli beam theory is assumed or bending moments are computationally approximated [42, 43]. Accuracy of the flexural response was governed by material parameters of the isotropic contribution of the strain energy function. Previous experimental work with pericardial tissue has recognized that the low-strain region is dominated by the ECM [43, 44]. For instance, uniaxial tensile testing performed on pericardia tissue after collagenase treatment demonstrated a striking reduction in the elastic modulus in the high-strain region, yet the effect the low-strain modulus was minimal [44]. In this aim, it has been shown that flexural analysis may provide a finer assessment of ECM elasticity than standard biaxial testing.

2.4.1 Mechanical Testing Modalities

Generally, it was observed that deflection optimization resulted in stiffer material parameters than those obtained from a purely biaxial approach. For some groups, parameter differences induced by the addition of flexural information significantly altered tissue deformation at physiologically-relevant levels of pressure. A previous investigation of mitral valve deformation which implemented bending stiffness of chordae and valve leaflets demonstrated significant changes to mitral leaflet flexure [45]. It was seen that the incorporation of appropriate bending stiffness eliminated the over-opening effect seen in the dynamic model of leaflet motion. Compared to the experimental leaflet deformation,

the computational model which utilized the correction to bending stiffness demonstrated higher accuracy. It is clear that multi-modal testing allows for greater characterization of soft tissue mechanics. In-plane compression testing of thin, fibrous soft tissue like pericardium is technically challenging; however, materials subjected to flexure undergo tensile and compressive loading. Cantilever bending benefits from utilizing simple geometry and loading conditions to implement large deformation. Furthermore, it has been demonstrated how this technique can be easily integrated with inverse material modeling within a computational framework to describe transversely isotropic materials.

2.4.2 Tissue Structure and Function

In this study, constitutive model parameters linked to the fiber properties were obtained from biaxial curve fitting and held constant during the bending optimization process. Previous work by Mirnajafi et al. showed that fiber orientation had minimal effect on the flexural response of native and chemically-treated bovine pericardium [43]. It was demonstrated here that inverse FEA is capable of capturing experimental flexure by means of tuning non-collagenous components of pericardia tissue. Structural constitutive modeling and computational tools allow for in-depth investigation of the relationship between tissue structure and mechanical function. The Holzapfel-type model presented here has been previously used to examine the contribution of matrix stiffness, fiber orientation, and fiber stiffness on stress concentration within bioprosthetic valve leaflets [46]. While the structural constitutive model formulation developed by Holzapfel et al. was originally used to describe the passive mechanical properties of arteries [39, 40], these forms can also be used to describe the behavior of planar, fiber-reinforced materials.

Through understanding the structure-function relationship of soft tissue, we may optimize bioprosthetic valve design and improve device performance.

2.4.3 Implications for Valve Design

Glutaraldehyde-treated bovine pericardium is recognized for its ideal mechanical properties and has been considered a standard source for bioprosthetic valve leaflets. However, some recent generations of valve designs have elected to use porcine pericardium. Porcine pericardium demonstrates similar mechanical characteristics with BP tissue; however, the thickness of porcine tissue is substantially reduced. The thinness of PP tissue lends itself to a more low-profile valve design, consequently improving the safety of transcatheter delivery. It can be seen from biaxial testing that PP is less compliant in both the preferred and cross-fiber directions. Construction of a virtual, generic TAV revealed that PP properties allowed for greater opening, potentially indicating an improvement to valvular hemodynamics during systole.

Even though differences in opening profiles occurred, the influence of tissue properties during diastolic closure needs to be investigated to obtain a clear picture of total valve performance. Considering the increased stiffness of PP tissue, it is expected that TAV designs will generally experience greater stress concentrations. Thus, a computational framework for design optimization would need to be established in order to explore the unique advantages of these pericardial materials.

2.4.4 Study Limitations

This is one of the first studies to successfully integrate mechanical testing modes into a single constitutive model of pericardial soft tissue; however, some limitations exist. Here, inverse FEA deflection was optimized to mimic the experimental deflection curve

under two loading conditions. Ideally, analysis of flexure under many load sets could help to further capture the material response; however, tight correspondence was observed between the two loading conditions performed. Furthermore, the moment-curvature description by Mirnajafi et al. only demonstrated a slightly non-linear response, indicating a relatively constant stiffness under flexural loading.

Accuracy of material model parameters was assessed by comparing deflection of beam bending. Qualitatively, this can be seen be seen by how well the computational deflection curves lie within the mean and standard deviation of experimental deflections. These material properties were subsequently applied to a generic TAV leaflet model and compared. It should be noted that an improvement in valve modeling accuracy may only be assumed; the TAV leaflet opening is not directly compared to experimental deformation. Future studies which employ flexural analysis may consider validation with experimental models of bioprosthetic valve pressurization.

Heterogeneous material properties may be a root cause of accelerated or asymmetric leaflet deterioration, therefore, it may be appropriate to investigate the effect of inter-leaflet material variability on TAV closure. In this aim, valve performance is only analyzed using a representative leaflet design. By taking a non-deterministic approach, the effect of geometry on TAV performance characteristics could be analyzed.

3 A COMPUTATIONAL FRAMEWORK FOR DESIGN OF TRANSCATHETER AORTIC VALVE LEAFLETS

3.1 Design Optimization, Robustness, and Uncertainty

The heart is an impressive structure due to its ability to withstand intricate mechanical loading and endure cyclic fatigue. Changes in geometry and material properties can have devastating effects on heart valve functionality. For example, incidence of AS and severity of calcification have been shown to increase as the number of native leaflets is reduced [5]. Areas of tissue degeneration leading to valve failure are commonly identified as regions of elevated stress/strain. Thus, it is important to understand the mechanical performance of prosthetic devices in order to ensure structural integrity over time.

From an engineering perspective, bioprosthetic aortic valves are well-suited for design optimization. The AV is subjected to a high-velocity jet throughout systole; however, during diastole, when the aortic valve is under greatest mechanical loading, blood flow is minimal. Thus, deformation of the AV during diastole may be approximated using static pressurization [41]. Small design defects or errors in implementation can be catastrophic, as revealed by the early destruction of Ionescu-Shiley valves. Transcatheter aortic valve replacement, while theoretically ideal, is predisposed to implantation uncertainties. Device performance under uncertain conditions is critical for delivering reliable, quality performance. Robustification of valve design can be achieved using modern computational analyses; however, finite element simulations of bioprosthetic heart valves has generally taken a deterministic approach [19, 38, 41]. In this aim, leaflet

geometry will be parameterized and relationships between design input and valve mechanics will be established. Design optimization will be carried out from an ideal deployment state and compared to a nominal valve design. Additionally, robustness-based optimization will be performed to identify leaflet constraints which minimize performance variability.

3.1.1 Strategies for Optimization

In metallurgy, the term *annealing* describes a process in which a material is heated, then gradually cooled so that atoms settle into a more ordered structure. The annealing treatment is able to increase ductility, thus making the material more workable. Adaptive Simulated Annealing (ASA) is a stochastic relaxation process based on the analogy of metal annealing. The ASA algorithm uses control of temperature schedules and random step selection to efficiently regulate parameter exploration. For parameters p^i with ranges $[A_i, B_i]$ in a N-dimensional parameter space, new design points, p_k^i, are generated by means of a distribution characterized by the product of distributions for the parameter, expressed in terms of temperatures and random variables y^i in $[-1, 1]$, where $p_k + 1^i = p_k^i + y^i(B_i - A_i)$. Each parameter's annealing schedule, T_i, is defined by

$$T_i = T_0 \exp(-ck^{1/N}) \tag{19}$$

where T_0 is the starting temperature. The ASA algorithm is appropriate for solving highly nonlinear problems with many potential solutions due to its ability to distinguish between local optima.

3.1.2 Strategies for Robustness and Reliability

In the context of engineering design, the term *robustness* describes the sensitivity of performance metrics to variations in design parameters. The objective in robust design is to improve product performance *and* reduce performance variability. Taguchi Robust Design, pioneered by Genichi Taguchi, is one method used to improve quality of manufactured goods. Taguchi characterized quality by employing a loss function, a continuous function defined in terms of variation of a performance factor from its target value. Founded on the principles of statistically designed experiments (DOE), Taguchi's parameter design approach generates an array of designs by combining levels of control and noise factors. Taguchi's methods were well received, especially in the industrial engineering community; however, some of the proposed statistical methods have been criticized by mathematicians.

Other approaches used to improve process or product improvement fall under the term *Six Sigma*. Six Sigma embodies a set of techniques whose formulations include uncertainty related to design parameters, objectives, and constraints. The name *Six Sigma* is derived from the concept that if one has six standard deviations between the mean target parameter and the nearest specification limit, there will essentially be no product failures.

3.1.3 Study Design

In this chapter, a general six sigma approach will be taken to evaluate the performance of the nominal and ASA-optimized leaflet designs under elliptical deployment conditions. A search method which combines ASA and six sigma will be described and employed to minimize performance variability of TAVs under eccentric expansion. Design exploration of TAV leaflets will follow the flow presented in Figure 21.

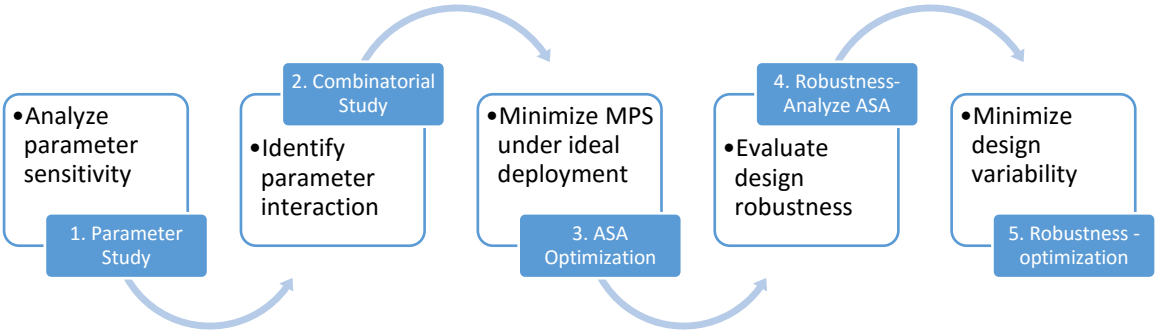

Figure 21. Flowchart of computational study of TAV leaflet design.

The framework described here encompasses the foundational description of leaflet geometry, efficient design optimization, and elegant robustification under TAV implantation uncertainty. In this way, a comprehensive analysis of leaflet mechanics can reveal fundamental characteristics to aid in the engineering of highly durable TAV devices.

3.2 TAV Leaflet Modeling

The first step in TAV leaflet design exploration is to efficiently describe a nominal geometry and use parametrized equations to model a reasonably large design space.

3.2.1 Leaflet Geometry Parameterization

A classic, crescent-shaped TAV leaflet geometry is adopted as the default design point. The characteristic leaflet has an attachment edge, also known as the suturing line, which is sewn along the stent and a free edge which coapts with adjacent leaflets. The shapes of the attachment edge and free edge were parameterized using the functions:

$$y = ae^{cx^2} \quad (20)$$

$$y_f = h(1 - \frac{e^{(x^3 - m^3)} - 1}{e^{(u^3 - m^3)} - 1}) \quad 21$$

Parameters *a* and *c* control the shape of the attachment edge; for simplicity, *c* is held at a constant value of 6.79. Variable *h*, representing the height of the free edge was described as:

$$h = y_{nom} + r(SSL - SSL_{nom}) \quad 22$$

When the length of the stent suturing line (SSL) is nominal, the height (*h*) is zero, indicating a straight free edge. As the SSL increase, the height of the free edge is raised to ensure proper valve closure. Values of nominal height (y_{nom}), nominal SSL (SSL_{nom}), and *r* were held constant at 13.3mm, 19.1mm and 0.377.

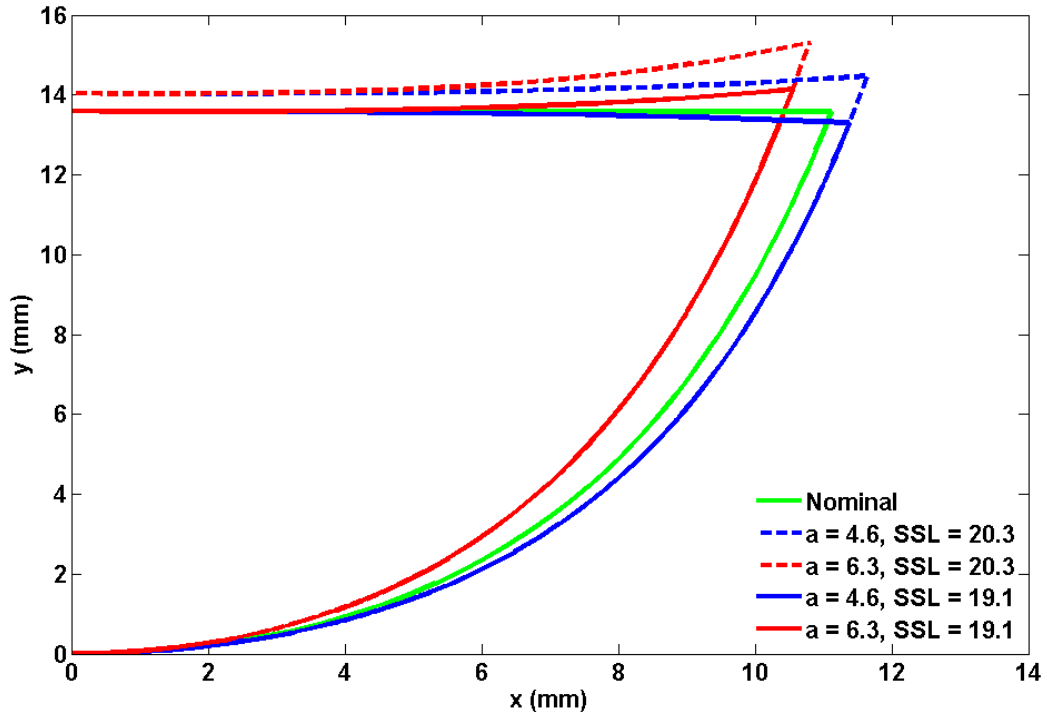

Figure 22. Geometric characterization of TAV leaflet with 2D shape parameter, a, and SSL.

The shape of the 3D attachment edge was characterized in cylindrical coordinates by the function:

$$z = pe^{b\theta} + qe^{d\theta} \qquad 23$$

Where *p*, *b*, *q*, and *d* are parameters controlling the attachment edge shape. For simplicity, *p*, *q*, and *d* are held at 1.79mm, 3.05E-08 mm, and 17.09, respectively. For each TAV design, SSL was conserved in 2D and 3D coordinate systems.

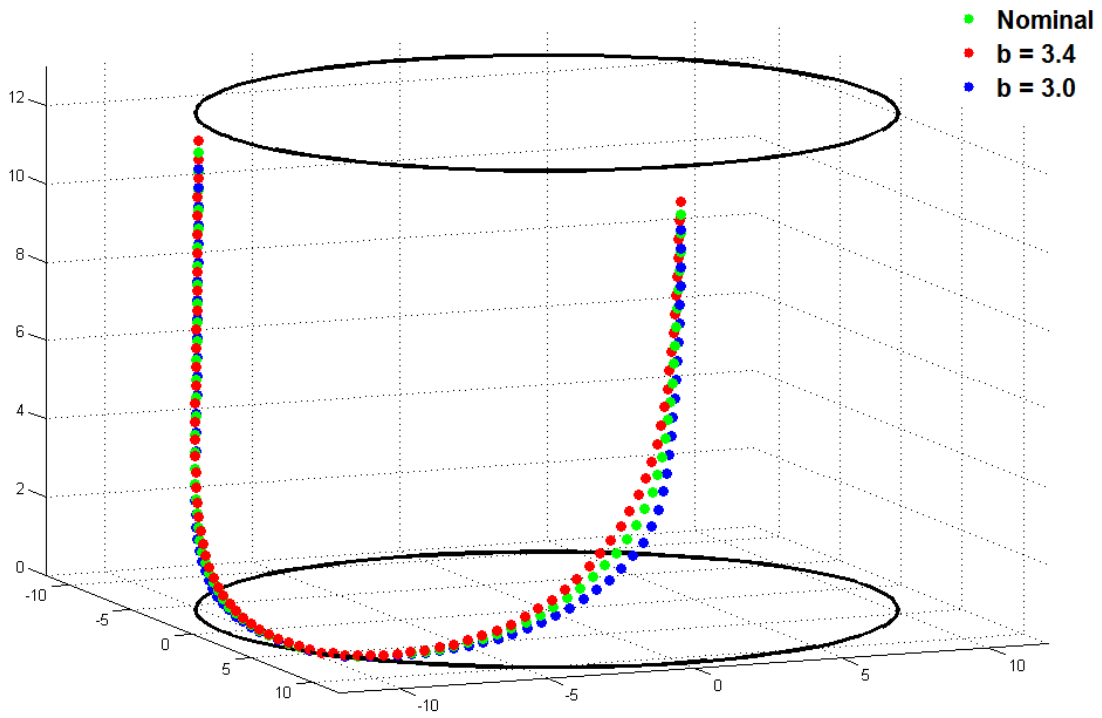

Figure 23. Effect of 3D shape parameter, b, on attachment edge shape. Black lines represent inner stent boundary.

As parameter *b* increases, the stent-leaflet attachment site becomes more oriented in the longitudinal direction. Conversely, reduction in *b* shifts the leaflet towards a wider, more rectangular configuration.

3.2.2 Virtual Assembly

After determination of the two-dimensional shape, new leaflet meshes were created using the thin-plate spline approach via custom Matlab (MathWorks, Natick, MA) code. Nodes within the updated boundary (free edge, attachment edge) were transformed using a flat, nominal-shaped leaflet mesh as the template.

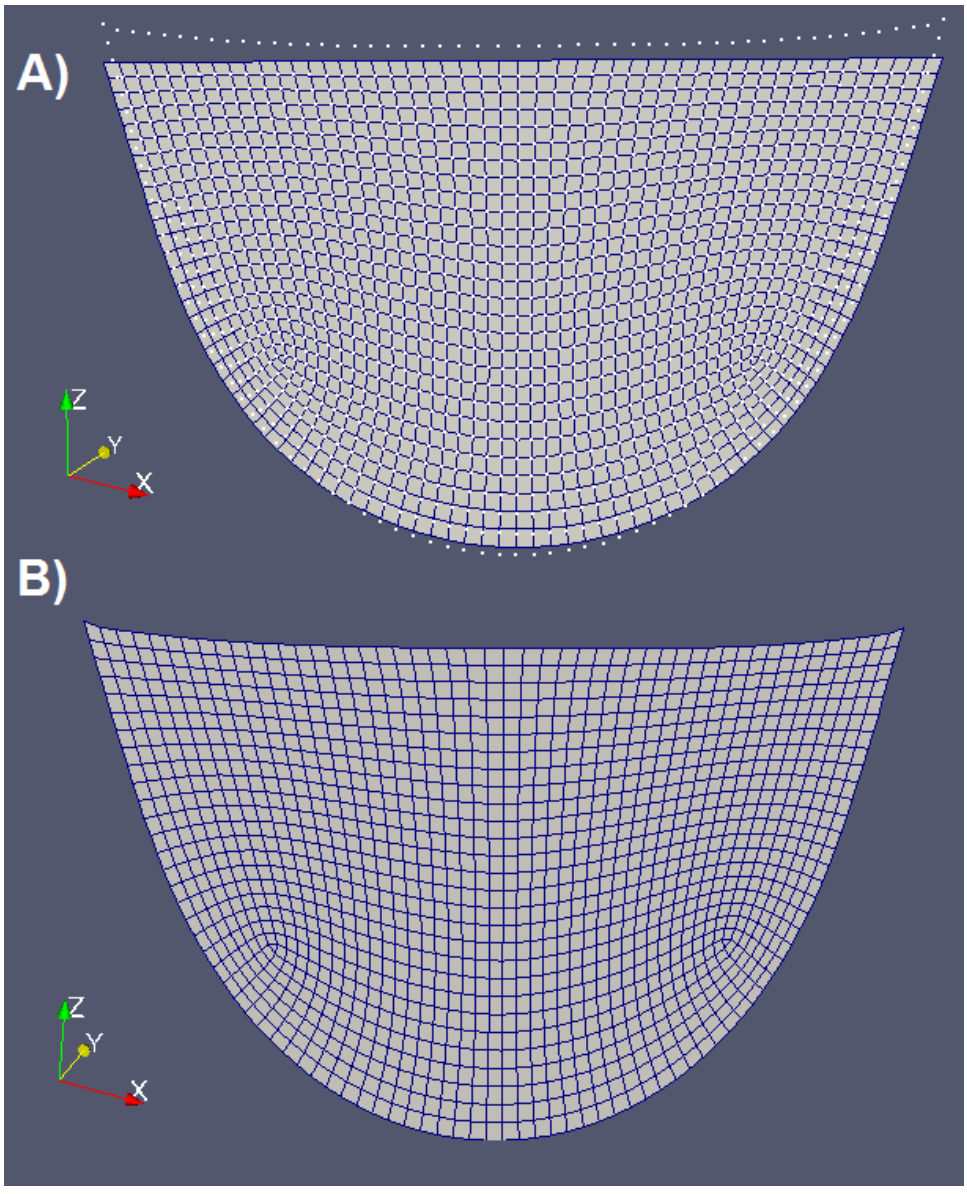

Figure 24. Illustration of TPS leaflet re-meshing. After specifying a template mesh (A), updated boundary nodes (white dots) are used to generate the target mesh (B).

Each leaflet was discretized into 1316 large strain shell elements (S4R and S3R finite strain elements with reduced integration) with a uniform thickness of 0.24 mm. The Abaqus Scripting Interface was used to update model file geometry through custom Python (Python Software Foundation, Wilmington, DE) scripts. The planar mesh was transformed into its 3D configuration by using finite element software Abaqus\Standard 6.13. The attachment edge coordinates were displaced to their 3D positions, calculated by Equation 23, and a small pressure is applied to the leaflet to facilitate convergence. The deformed leaflet shape was rotated ± 120° to create the remaining two leaflets with symmetry. Hence, the final, stress-free valve structure was constructed via virtual assembly method.

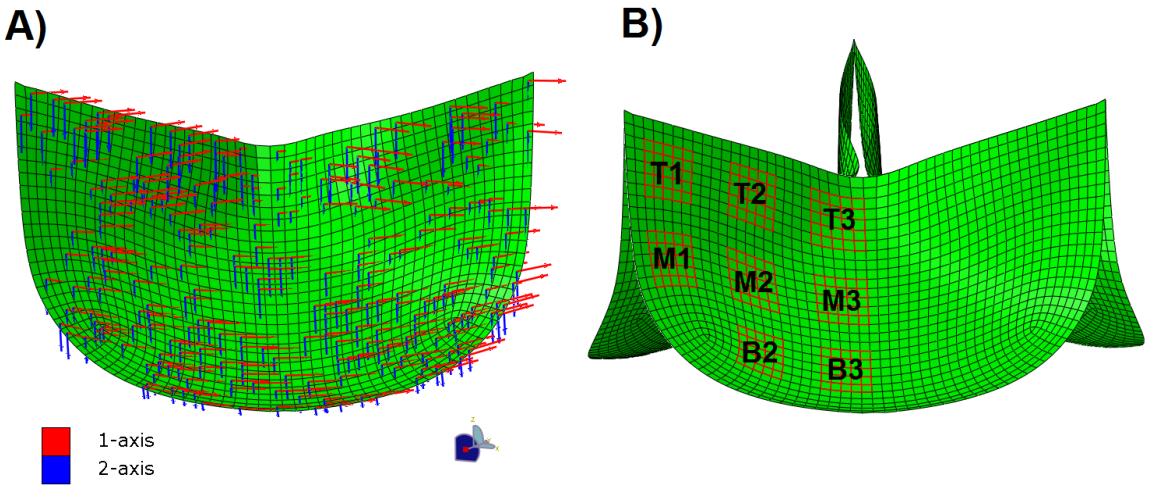

Figure 25. Material orientation axes (A) were defined in the radial (blue) and circumferential (red) directions. Node and element sets (B) were defined across the leaflet to monitor stress and contact distribution.

The material axes, as displayed in Figure 25, were defined such that the preferred-fiber direction was oriented circumferentially and the cross-fiber direction was oriented radially. Peak stress from the assembled TAV, total contact area between neighboring leaflets, maximum principle stress from specific regions (i.e. T1, M1, etc.) and contact area within the T-regions (T1, T2, T3) were output from closure simulations. Additionally, the standard

deviation (M_{std}) of stress from the M-regions (M1, M2, M3) and standard deviation of contact area (C_{std}) in the T-regions were used to quantify the distribution of stress across the belly and contact along the free margin, respectively.

3.2.3 Finite Element Analysis

The hyperelastic material model parameters of BPN and PPK were applied to TAV leaflets using a UMAT subroutine and a coefficient of friction of 0.1 was assigned to each leaflet [38, 41]. TAV closure was performed by applying a uniform pressure of 120 mmHg to the aortic side of the leaflets. For leaflet closure under ideal stent deployment, a stent frame was not included in the FE assembly. Instead, nodes along the attachment edge were fixed from displacement to simulate its rigid boundary.

For leaflet closure under a sub-optimal stent deployment, a simple, thin-walled tube was used to model a generic stent. A tie constraint was defined between nodes along the attachment and inner surface of the stent. In this way, only four node sets along the height of the stent were need to displace the leaflet boundary into an elliptical shape. The four node sets, as shown in Figure 26, are used to control the long and short axes of an ellipse.

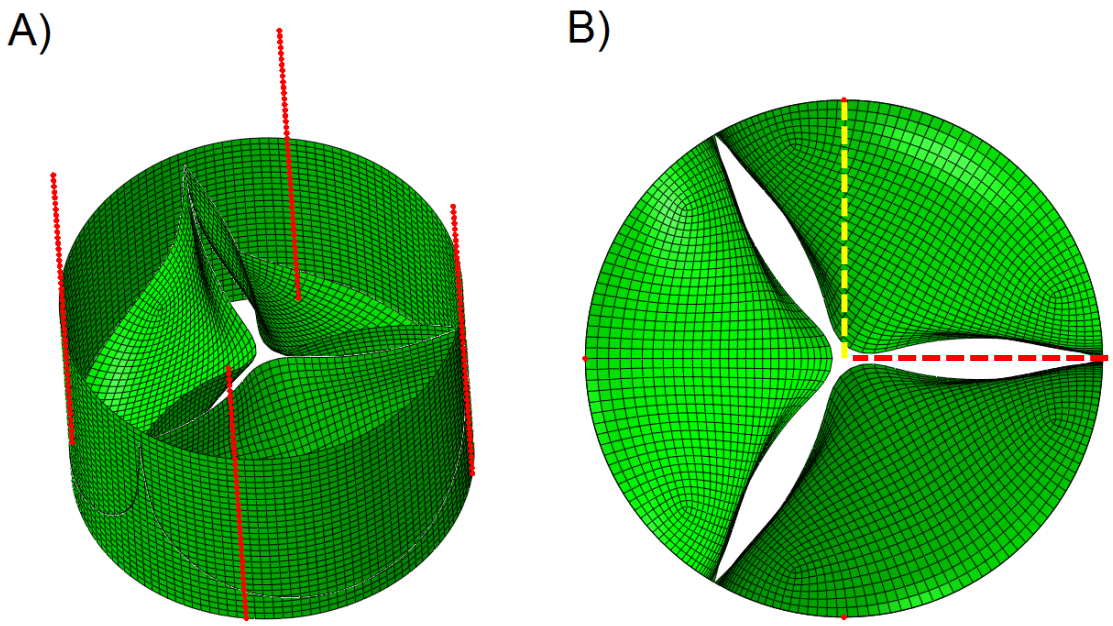

Figure 26. Oblique (A) and top (B) view of boundary conditions used to create an elliptical boundary. The red and yellow dashed lines represent the long and short axis, respectively.

The displacement of the long and short axes were calculated using the equation of eccentricity.

$$e = \sqrt{1 - \left(\frac{b}{a}\right)^2} \qquad 24$$

Where b and a are the lengths of the long and short axes, respectively. When the axes lengths are equal, *e* approaches zero; conversely, when one axis dominates, the shape approaches a straight line. Three distinct eccentricity distributions, shown in Figure 27, were chosen to represent three generic deployment possibilities.

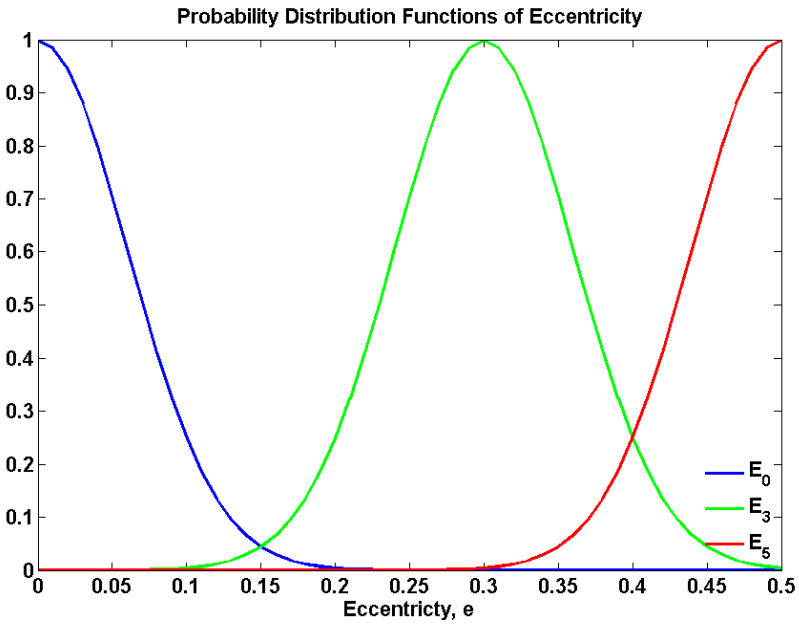

Figure 27. Normal distributions of eccentricity values to represent likelihood of elliptical deployment.

3.2.4 TAV Design Space

Process automation software Isight was used to explore the design space. The Design of Experiment, Optimization, and Six Sigma components were chosen for their broad selection of design-search techniques. The Parameter Study and Full Factorial methods were used to investigate individual parameters and interaction effects, respectively. Each parameter range was segmented into 30 increments and both analyses were performed for leaflets defined by BP and PP material properties. The ASA method was selected in the Optimization component and the maximum MPS value was set as the object function. A detailed analysis of the optimization framework is shown in Figure 28.

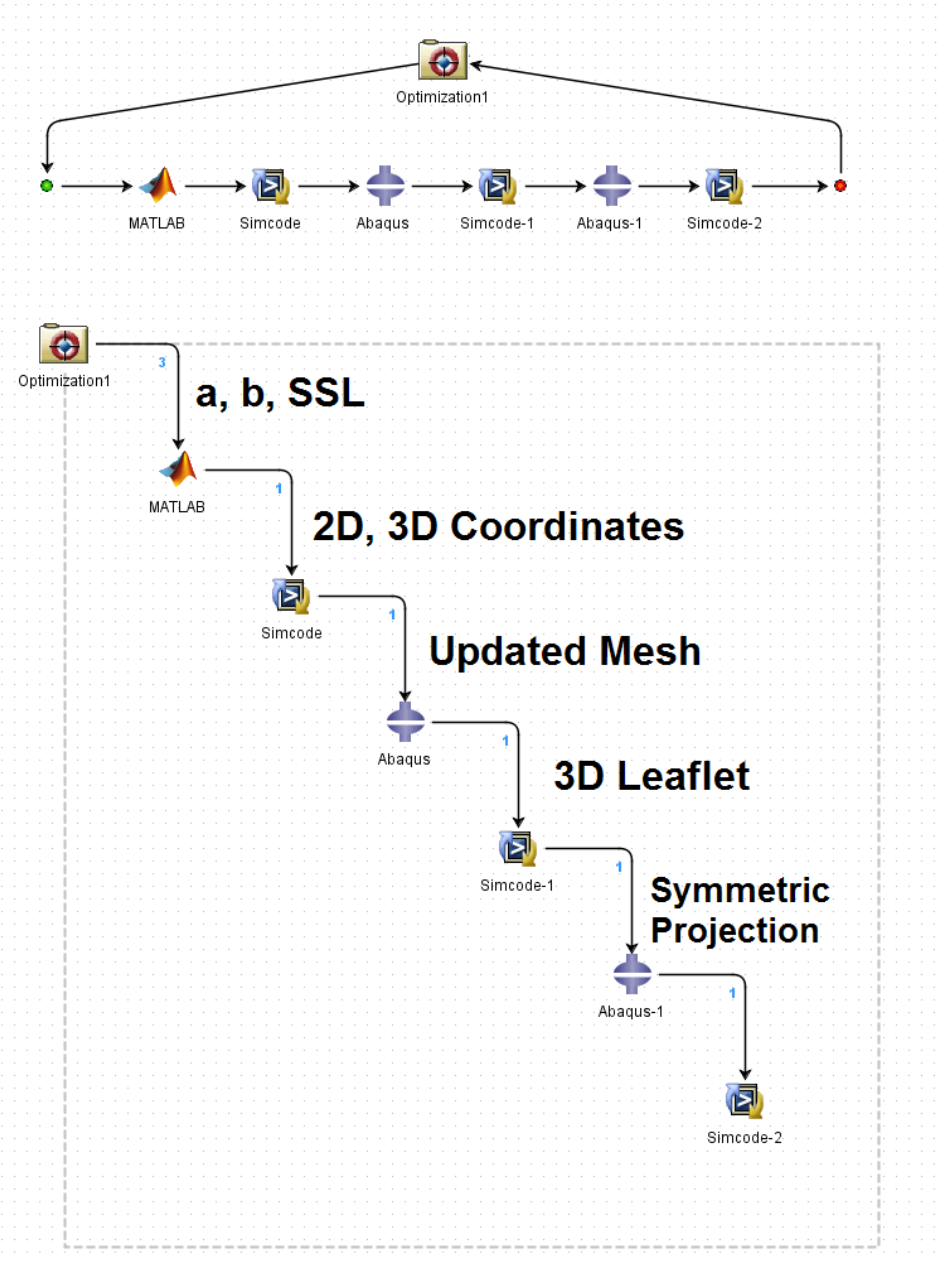

Figure 28. ASA optimization framework layout (top) and breakdown of component outputs (bottom).

The maximum number of allowable runs was set to 300 for BP and PP leaflets. As seen in Figure 28, Isight supplies new values for design variables a, b, and SSL. Matlab is used to determine the updated attachment and free edge boundaries in 2D. The target mesh is generated using TPS re-meshing and the node coordinates are read into Python (*Simcode*).

Python updates the Abaqus leaflet model and the 2D-to-3D transformation is performed. The new 3D leaflet coordinate values are read in Python and the three leaflet geometries are updated, thereby ensuring inter-leaflet symmetry. The TAV assembly is pressurized as previously described and Python extracts the desired output metrics.

The layout of the elliptical optimization scheme is presented in Figure 29. TAV leaflets are generated in an identical manner as described above.

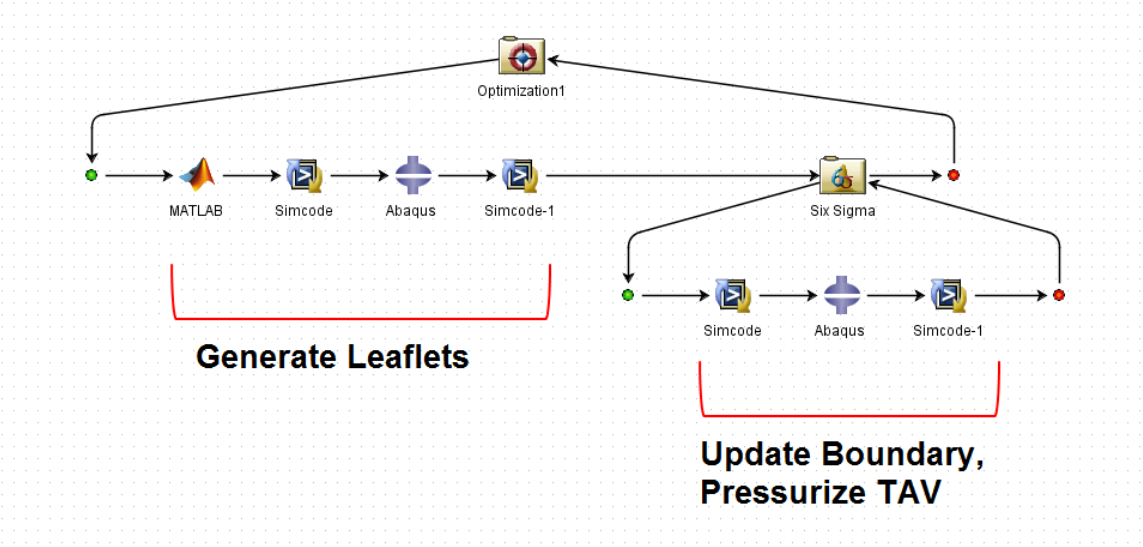

Figure 29. Robust-optimization arrangement. TAV leaflets are generated as previously described (left), elliptical boundaries are generated (right), and diastolic pressurization is performed. The mean and standard deviation of MPS is output from the Six Sigma module to the Optimization component.

The 3D leaflet geometry was updated in each run and the Six Sigma component employed Monte Carlo sampling to determine 10 eccentricity values from the appropriate probability density function, shown in Figure 27. Python updated the node set displacements using Equation 24. The mean and standard deviation from the ten runs were exported to the ASA component and the next design point was determined. A total of 50 designs were evaluated for each eccentricity distribution and only BP material parameters were used in this analysis.

3.3 Parameterization Study and Combinatorial Design

Diastolic pressurization of TAV leaflets resulted in reasonable structural deformation. The nominal design of a generic BP and PP leaflet resulted in stress concentrations near the belly of the leaflet, towards the attachment edge. Maximum principle stress for PP leaflets, 199.8 PSI, was notably higher than BP leaflets, 183.7 PSI of the same thickness. Since biaxial tensile testing demonstrated a significant reduction in compliance of PP tissue in both the preferred-fiber and cross-fiber directions, this observation is not surprising. Maximum stress consistently peaked in the belly near the transition to the contact region, yet decreased rapidly within the contact area.

The parameter study revealed significant effects of input variables on several output parameters; however, these relationships were not identical between BP and PP leaflets. Some output parameters were also well correlated with each other. The most notable relationship observed was the dependence of leaflet MPS on distribution of stress along the M-region. As shown in Figure 30, once stress concentration along the belly became well-distributed, i.e. M_{std} was reduced, maximum principle stress in the leaflet was minimized.

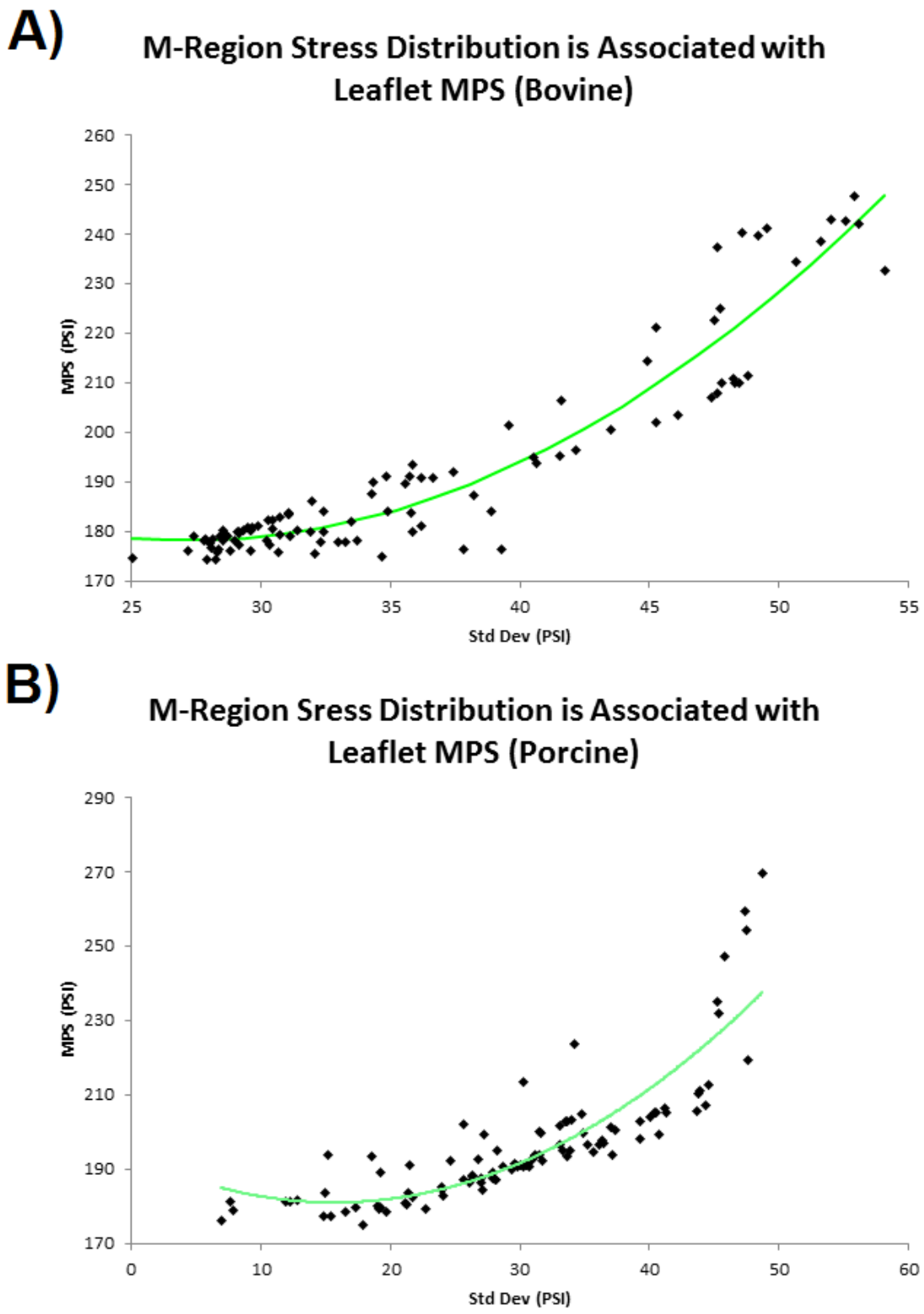

Figure 30. Distribution of stress in the M-regions was strongly correlated with the maximum principles stress of the entire leaflet. The data trendline is drawn in green.

It is believed that stress distribution along the belly is important for AV mechanics due to the natural alignment of collagen fibers in native AVs. The computational results shown here further establish the significance of this relationship. Furthermore, distribution of stress tended to be increased in PP leaflets compared to BP. Differences in stress concentrations are likely attributed to the differences in material properties between bovine and porcine pericardia. It is understood that collagen orientation across valve leaflets is important for mechanical performance; however, it may be a pivotal factor when considering device optimization. Generally, it was observed that SSL strongly influenced stress along the middle and bottom portions of the leaflet.

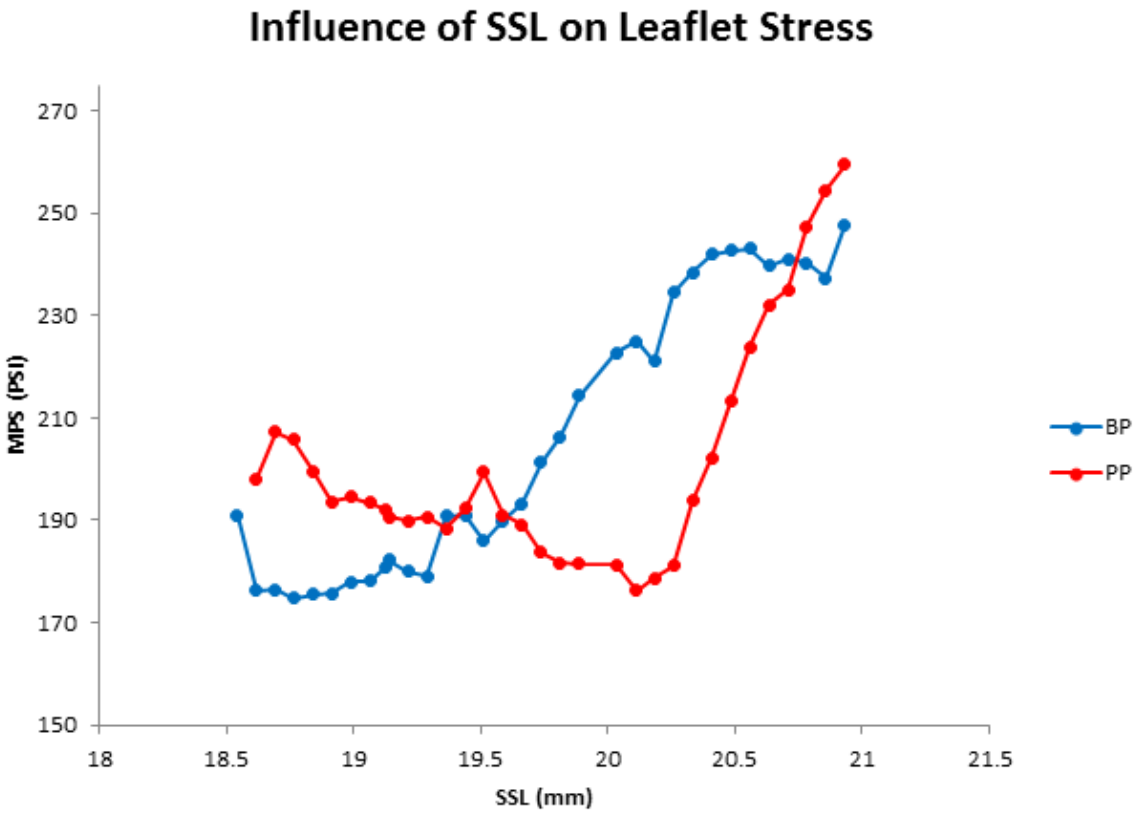

Figure 31. Effect of SSL on total leaflet MPS.

As demonstrated by Figure 31 and Figure 32, respectively, SSL controlled the MPS of the leaflet and distribution along the belly.

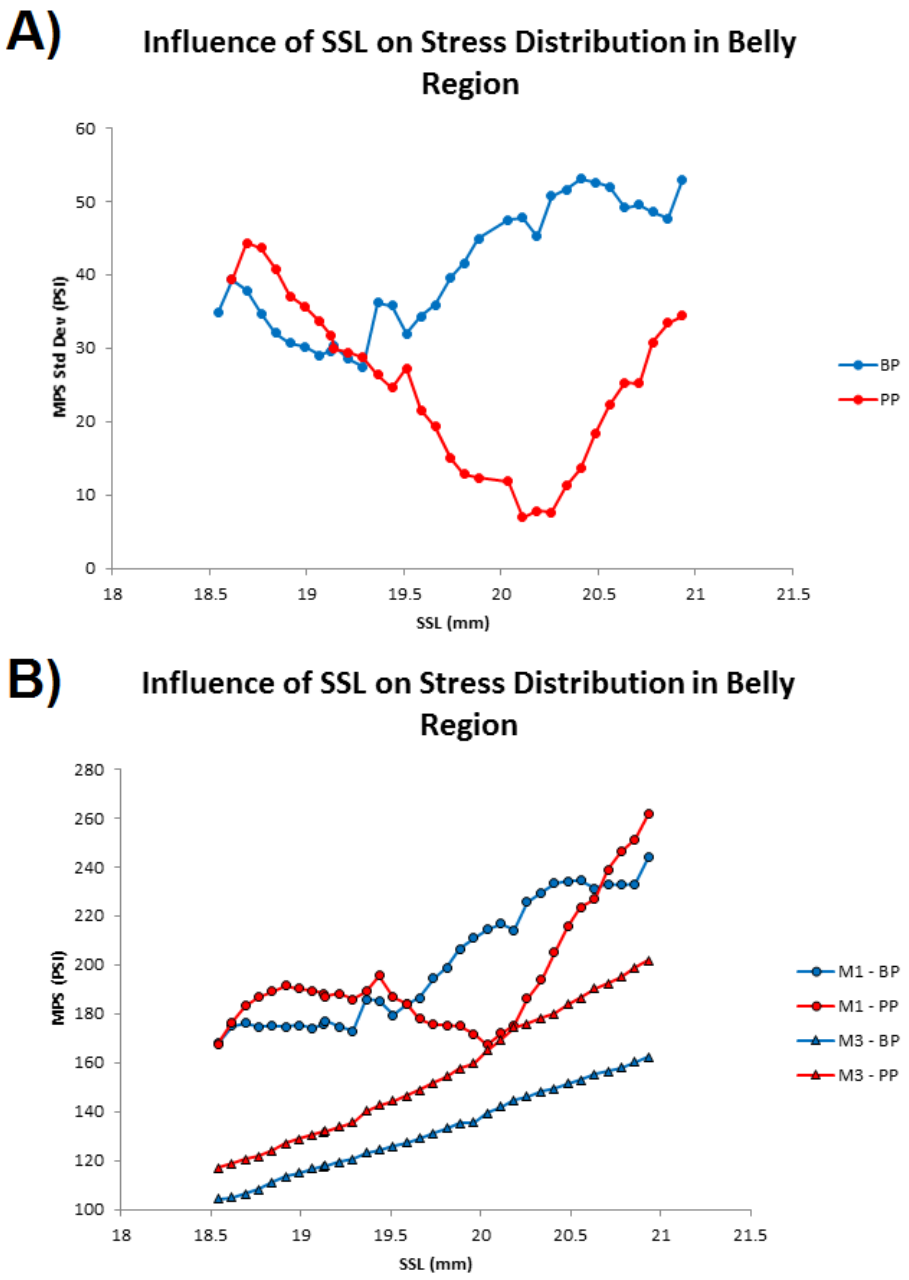

Figure 32. Effect of SSL on stress distribution in the M-region. Stress distribution, M_{std}, (A) was influenced by SSL in a material dependent manner.

The 2D attachment shape parameter generally influenced stress near the free margin, i.e. the T-region, and leaflet-to-leaflet contact area. As summarized in Figure 33, increasing the width of the 2D shape gradually increased the magnitude of contact area and tended to decrease stress near the free edge.

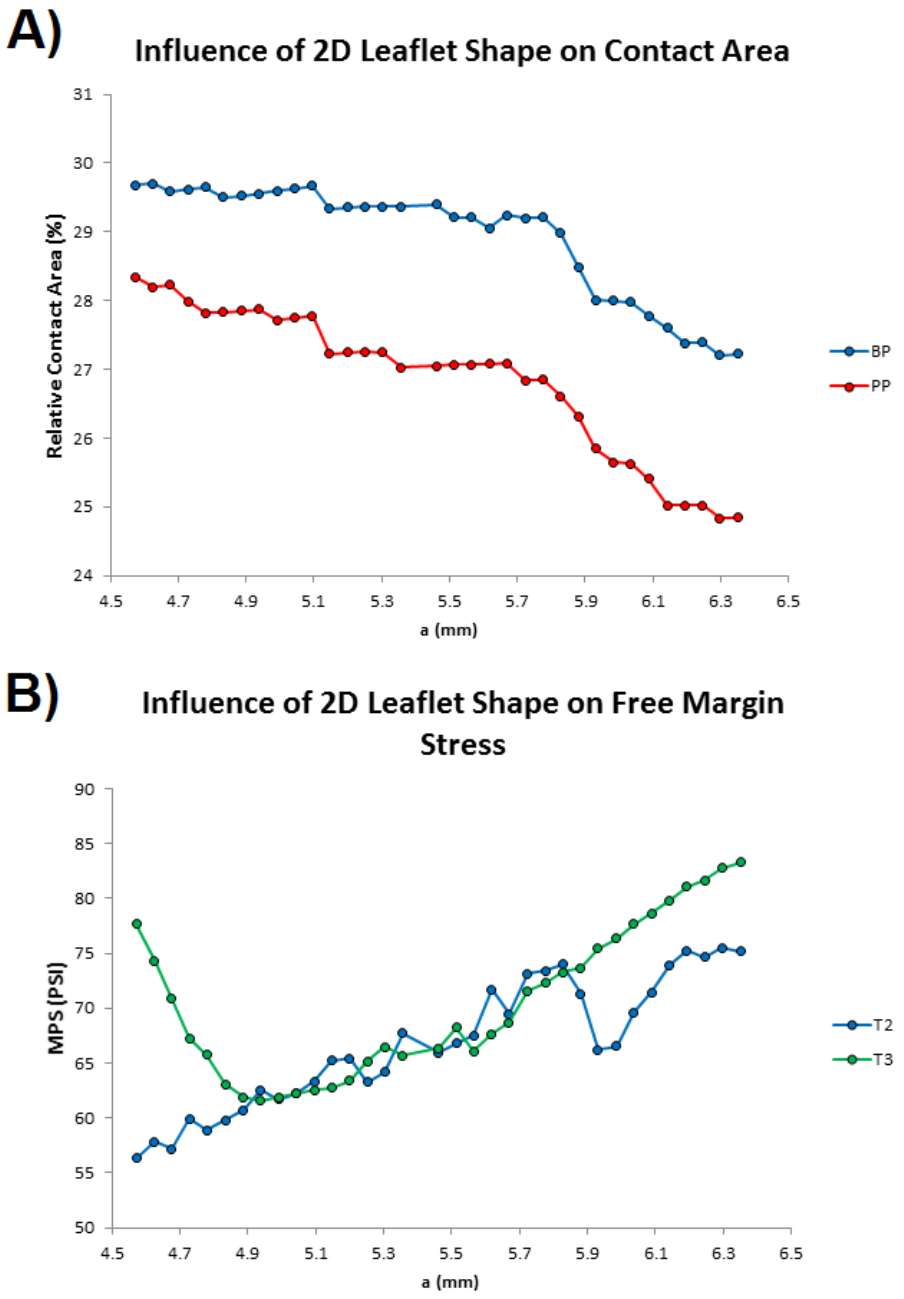

Figure 33. Effect of 2D leaflet shape on contact area (A) and stress concentrations (B), only BP shown.

The 3D attachment shape parameter, b, also tended to control contact area and stress concentrations near the free edge and belly. As shown in Figure 34, contact area steadily increased as the leaflet edge became wider and stress was progressively lowered in some areas.

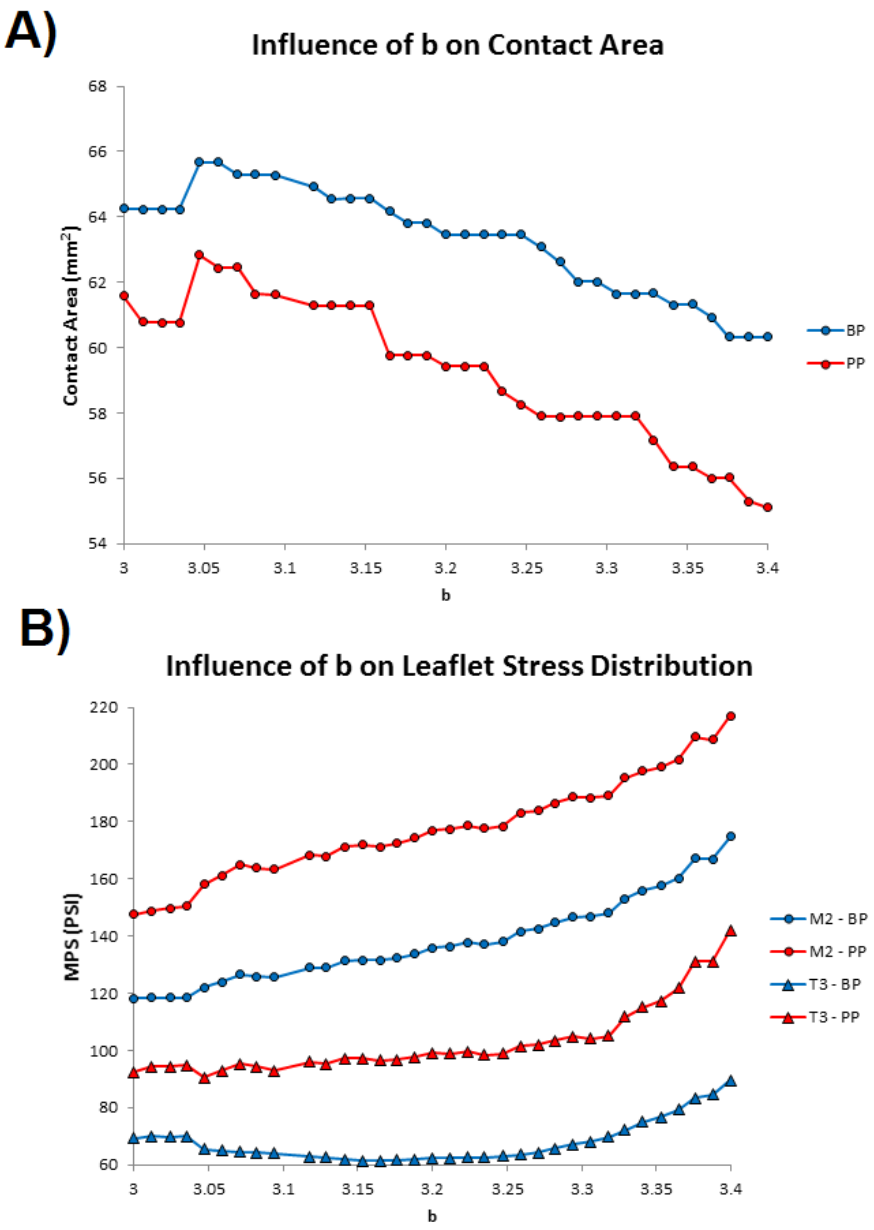

Figure 34. Impact of 3D attachment shape on leaflet-to-leaflet contact area (A) and stress concentrations (B).

Patterns observed during the parameter study provide support for the notion that stress and inter-leaflet contact are readily modulated by moderate changes in leaflet geometry and material characteristics. In order to efficiently approach an optimization investigation, a full factorial study was performed to provide insight into appropriate ranges for input parameters. Figure 35 demonstrates how the relationship between SSL and leaflet MPS

changes with respect to the 3D attachment edge shape. For both material properties, a shorter SSL was favored for a wider attachment edge design and a higher SSL was beneficial with a narrower attachment edge. Since increases in 2D leaflet area and broadening attachment edge shape increases contact area, these results indicate that maximizing leaflet coaptation may not result in minimal leaflet stress concentration.

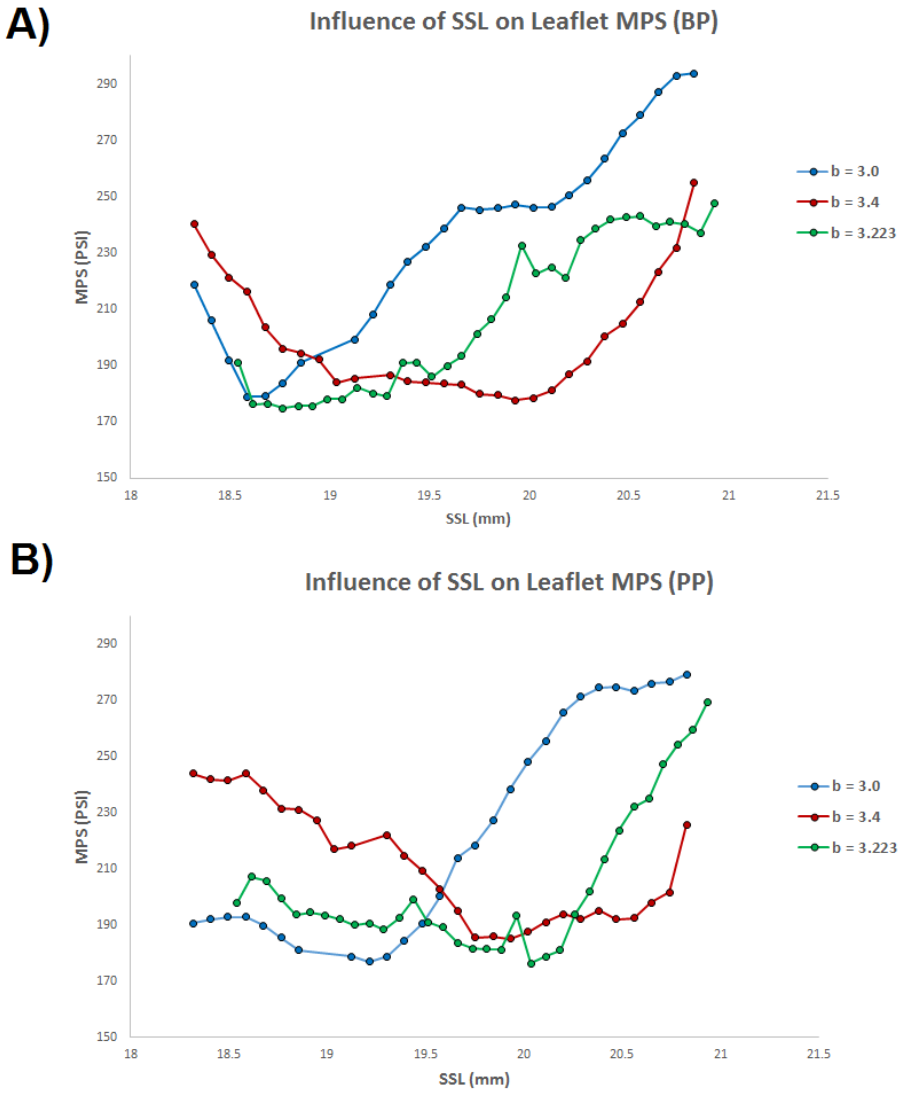

Figure 35. Interaction between *b* and SSL on leaflet MPS.

Generally, the 2D shape parameter, *a*, played a more minor role in development of leaflet stress compared to the 3D attachment shape.

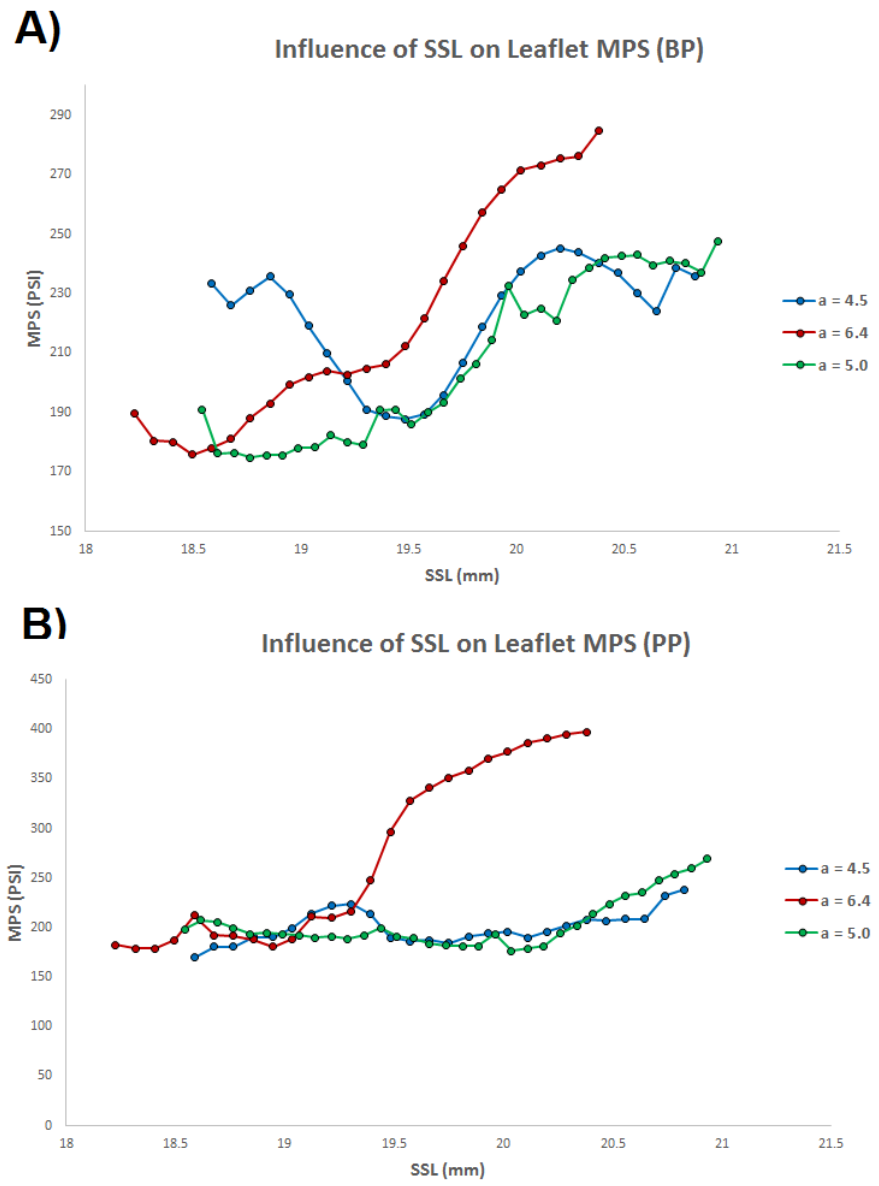

Figure 36. Interaction effect between *a* and SSL on maximum principle stress.

Notable difference between the two material models developed as the 2D leaflet approached a tapered, elongated shape. When the commissure peaks extended vertically, stress concentrations also emerged along the free edge. The inclined edge experienced high tension during pressurization in addition to focal stress along the belly. The results taken from the single-parameter and combinatorial studies reveal significant relationships

between design parameters and output variables. Some of the observed interactions can be seen in Figure 37.

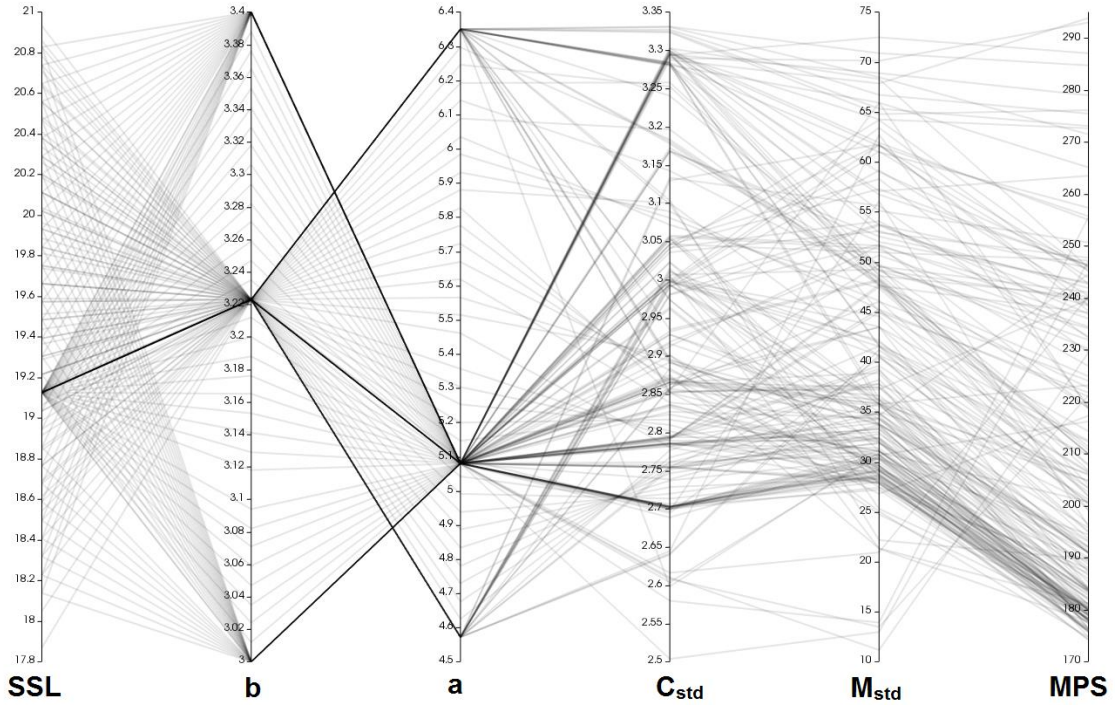

Figure 37. Parallel coordinate graph of input parameters and key output metrics. C_{std} and M_{std} is the standard deviation of contact area in the T-regions and stress in the M-regions, respectively. Output values only reported from BP leaflets.

Independent of material model, the maximum principle stress during TAV pressurization was strongly correlated with the uniformity of stress along the leaflet belly. Stress distribution, in turn, was usually associated with uniformity of contact along the free edge width. Observation of local minima at various parameter combinations prevented significant restrictions from being made to the parameter space for optimization studies.

3.4 TAV Leaflet Optimization

Shape optimization of TAV leaflet geometries resulted in a significant reduction in maximum principle stress for bovine and porcine material models. The ASA optimization

thoroughly explored the design space, as seen by the parameter histories shown in Figure 38 and Figure 39.

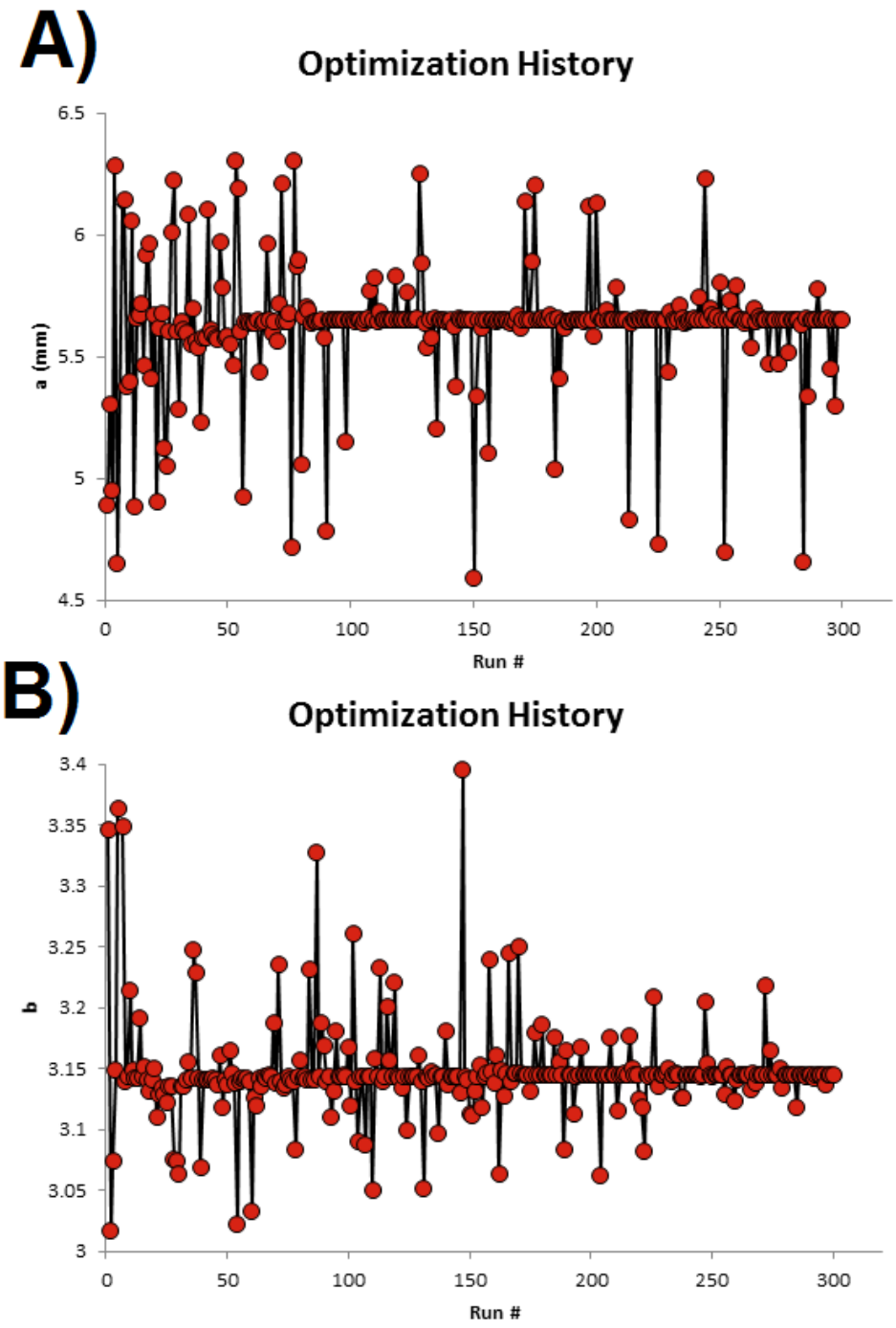

Figure 38. Search history of parameters a (A) and b (B) demonstrated convergence of optimization (PP material model).

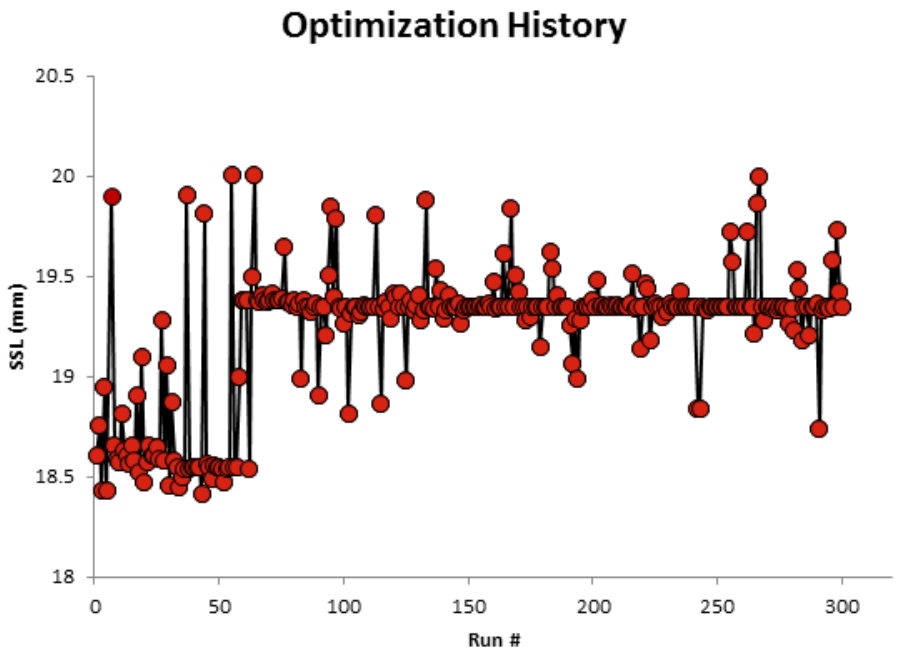

Figure 39. History of SSL during leaflet optimization (PP material model).

The geometric design parameters resulting in lowest peak stress are presented in Table 3.

Table 3. Design comparison of nominal and optimized leaflet geometries.

Design	a (mm)	b	SSL (mm)	MPS (PSI)
BP – Nominal	5.08	3.223	19.126	183.7
PP – Nominal	5.08	3.223	19.126	199.8
BP – Optimal	5.7379	3.2085	19.21	162.5
PP – Optimal	5.6515	3.1449	19.3446	165.3

Even though observable differences were reported between BP and PP material models in the parameter study, shape optimization resulted in similar geometric design points. For both materials, maximum principal stress was reduced most when the attachment length and width were was slightly increased. Nominal and optimized geometries are compared in Figure 40.

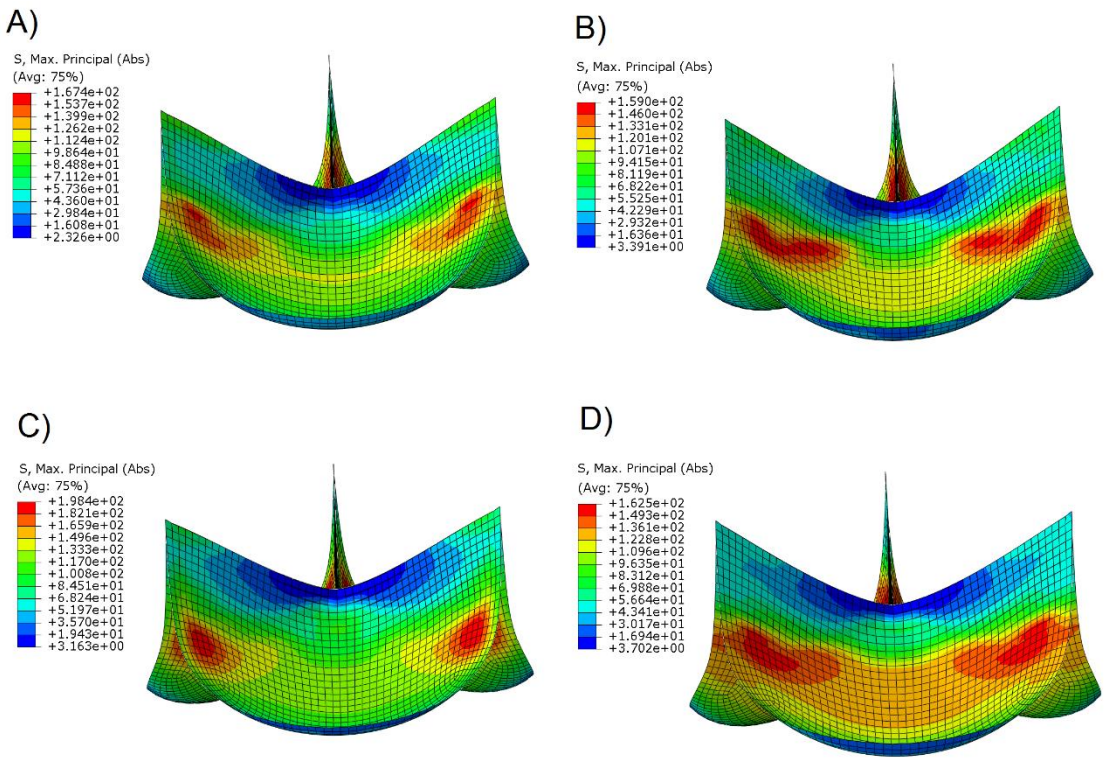

Figure 40. Comparison of nominal (A, C) and optimized (B, D) designs for bovine (top) and porcine (bottom) leaflet materials under diastolic pressurization.

Under nominal design conditions, both leaflet materials demonstrate peak stress concentration in the belly region, near the attachment edge. After geometric optimization, BP and PP leaflets achieved much greater stress distribution in the circumferential direction. As seen in the parameter study, PP leaflets were capable of a higher degree of stress dispersion than BP leaflets. As a result, PP design benefited from geometric optimization greater than its bovine counterpart. A response surface plot, shown in Figure 41, further elaborates the relationship between input parameters and leaflet stress.

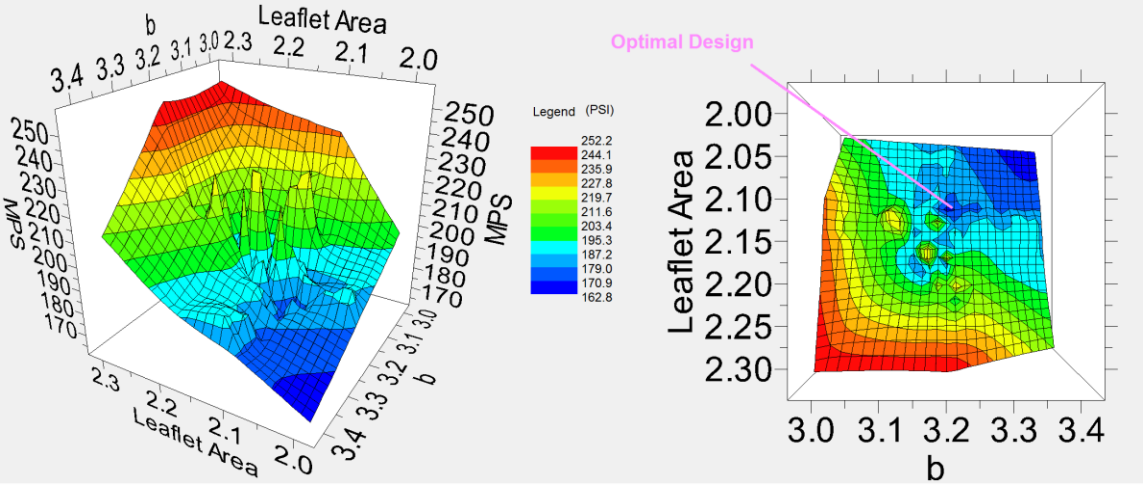

Figure 41. Response surface plot of 2D leaflet surface area (cm^2), attachment edge shape parameter, and max principle stress (PSI) using BP material parameters. The design resulting in lowest MPS is highlighted in pink.

Generally, peak stress was concentrated when leaflet surface areas became relatively large. When leaflet size increased, the line of contact was lowered and contact area increased. Since stress concentration tended to develop beneath the lowermost contact zone, increasing the contact triangle's depth created a sharp stress gradient. This observation, taken with Figure 37, demonstrates that the shape of the leaflet-to-leaflet contact area may be an important characteristic for establishing circumferential stress distribution. This type of relationship can be easily investigated using computational tools; however, experimental validation is needed to confirm such an important leaflet deformation characteristic.

3.5 TAV Leaflet Robustness

Geometric optimization of TAV leaflets successfully reduced peak stress concentration; however, the circular attachment boundary represents an idealized deployment condition. Robustness-based optimization was performed to find leaflet designs which could withstand diastolic closure after eccentric deployment. The design

parameters for each eccentricity distribution which resulted in lowest peak stress are presented in Table 4.

Table 4. Design parameters from robust optimization.

Design	a (mm)	b	SSL (mm)	2D Area (cm^2)
Nominal	5.08	3.223	19.13	2.259
E_0 Opt	6.309	3.3839	18.483	2.066
E_3 Opt	6.086	3.3131	19.280	2.201
E_5 Opt	5.433	3.3797	19.005	2.211

Similar to the result shown in the ASA optimization, leaflet designs with small leaflet surface areas and narrow attachment shapes resulted in the lowest, least variable stress concentrations. However, the 2D surface area of optimal leaflets tended to increase with eccentricity, possibly indicating a minimal leaflet size to ensure proper valve closure. As eccentricity increased, a narrow, vertically-oriented 3D attachment shape was preferred. The performance of the nominal and ASA-optimized leaflet designs are compared to the robustness-optimized leaflets in Figure 42.

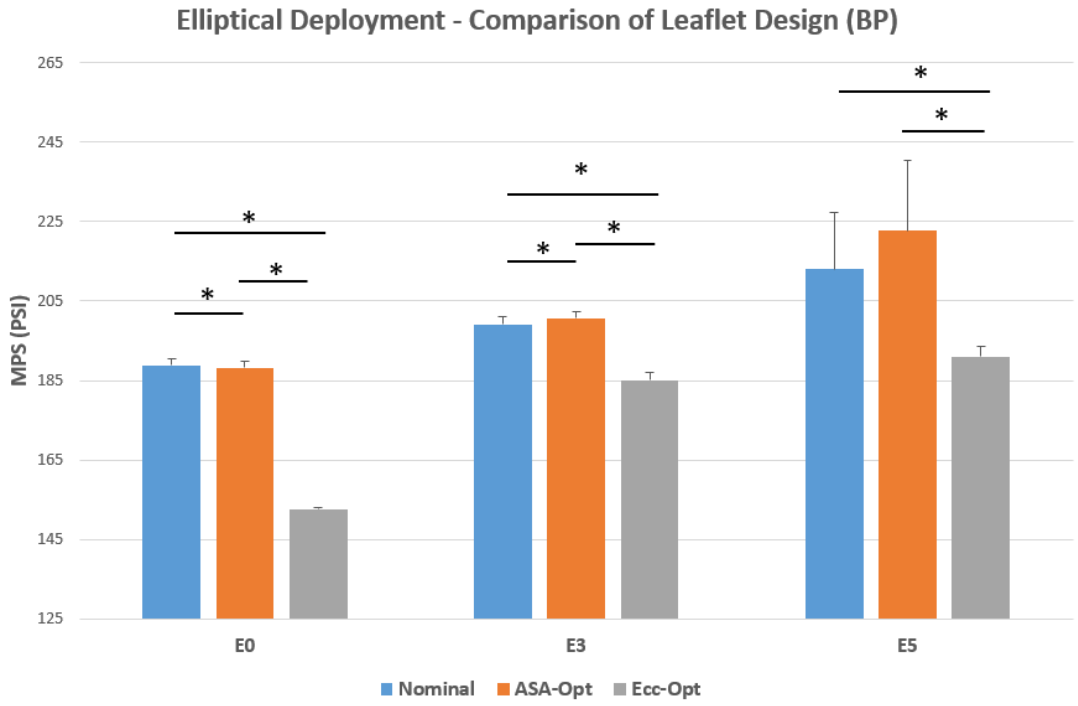

Figure 42. Comparison of valve design performance under elliptical deployment distributions. Orange and gray bars represent the ASA-optimized and robustness-optimized designs, respectively. Error bars represent standard deviation and asterisks indicate significant differences, $p < 0.05$.

Robustness-based optimization of TAV leaflet geometries revealed shapes with significantly reduced stress concentrations. In addition to reducing the average peak stress, the elliptical-optimized designs demonstrated less variability, most notably in the E_5 distribution. It was seen in Figure 41 that the optimal design point occurred in a localized region of the design space. Analysis of this design under elliptical deployment showed that even small changes to the attachment boundary shape can annul its improvement to the nominal leaflet geometry. Thus, it may not be appropriate to perform leaflet shape optimization under idealized TAV geometry. Even though robustness-based optimization was able to find leaflet designs with minimized peak stress concentrations, MPS increased significantly with eccentricity. Optimized geometries, shown in Figure 43, demonstrated peak stress locations along the belly, near the M1 region.

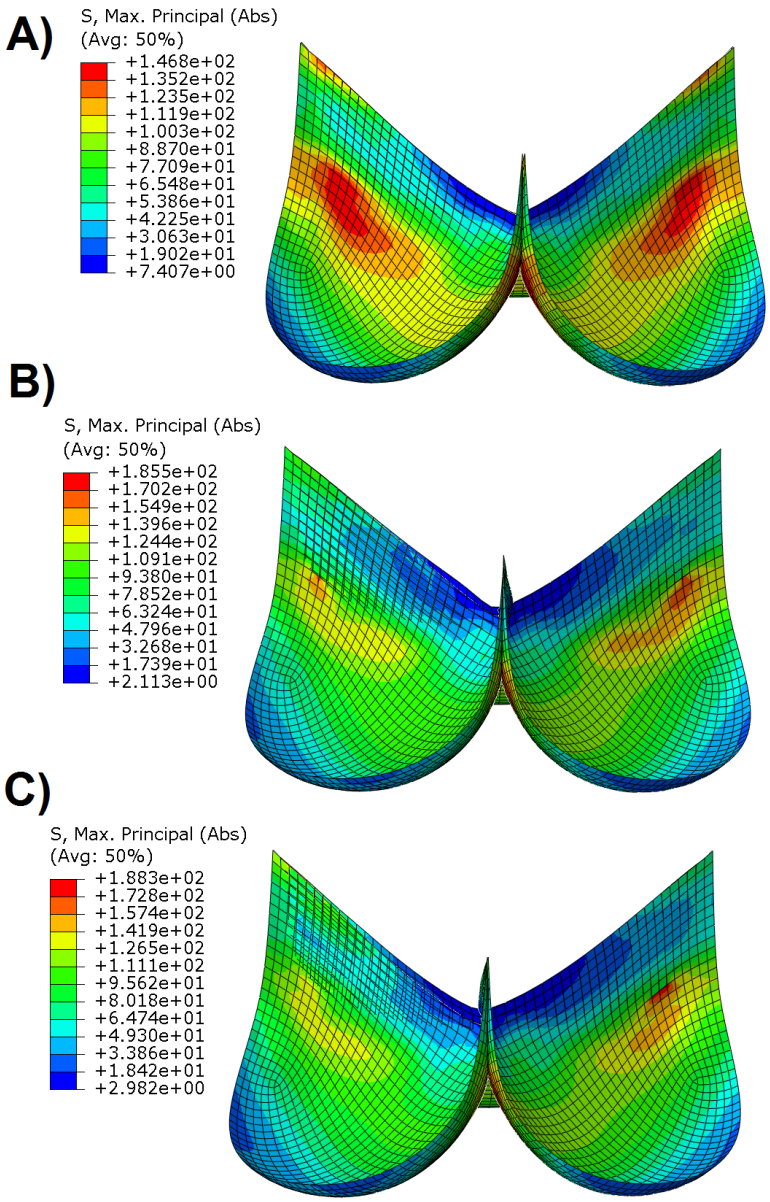

Figure 43. Optimal leaflet designs under E_0 (A), E_3 (B), E_5 (C) eccentricity distributions.

Asymmetric stress distributions began to occur at eccentricities greater than approximately 0.3. Peak stress concentrations tended to appear on the non-collapsing leaflets, along the belly where contact with the collapsed leaflet terminates. Contact area along the free margin was reduced during elliptical deployment, as seen in Figure 44, and commissure strain generally increased with eccentricity.

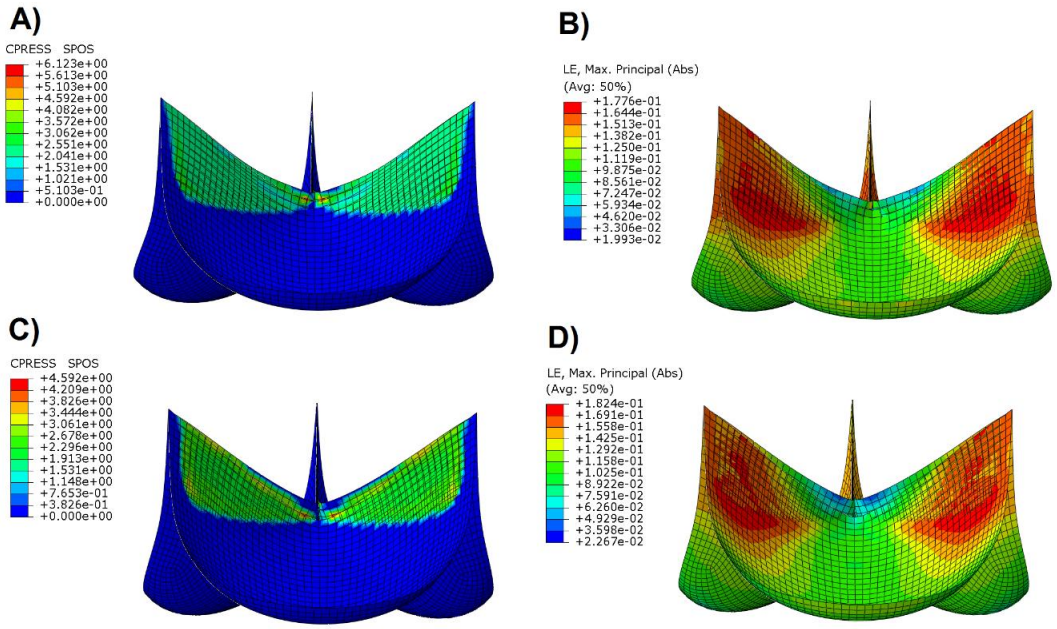

Figure 44. Contact area (left) and MPE (right) for E_3 (top) and E_5 (bottom) optimal leaflet designs.

The relationship between belly stress distribution and peak leaflet MPS was also observed during the robustness optimization. Figure 45 illustrates the strong correlation between MPS and distribution of stress across the collapsing and non-collapsing leaflets.

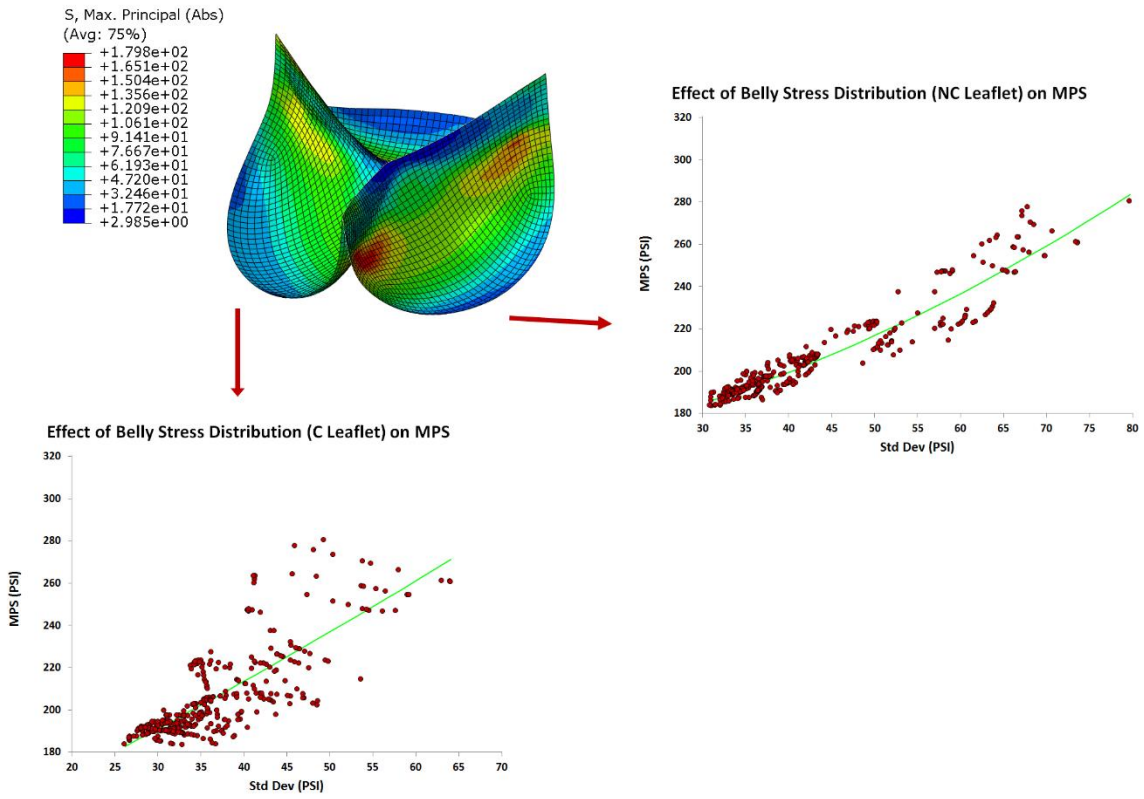

Figure 45. Representative valve design under elliptical closure (e = 0.3). MPS of the TAV is correlated with M-region stress distribution in the non-collapsing leaflet (right) and collapsing leaflet (left).

Peak stress during TAV pressurization under elliptical conditions occurred on the non-collapsing leaflet, thus, stress dispersion along this leaflet was most closely related to leaflet MPS. As previously implied, stress distribution may be more strongly effected by contact area shape as contact magnitude. Figure 46 shows how contact between the collapsing and non-collapsing leaflets was related to stress distribution. As seen in the circular-orifice optimization, uniformity of contact along the free margin tended to promote circumferential stress distribution.

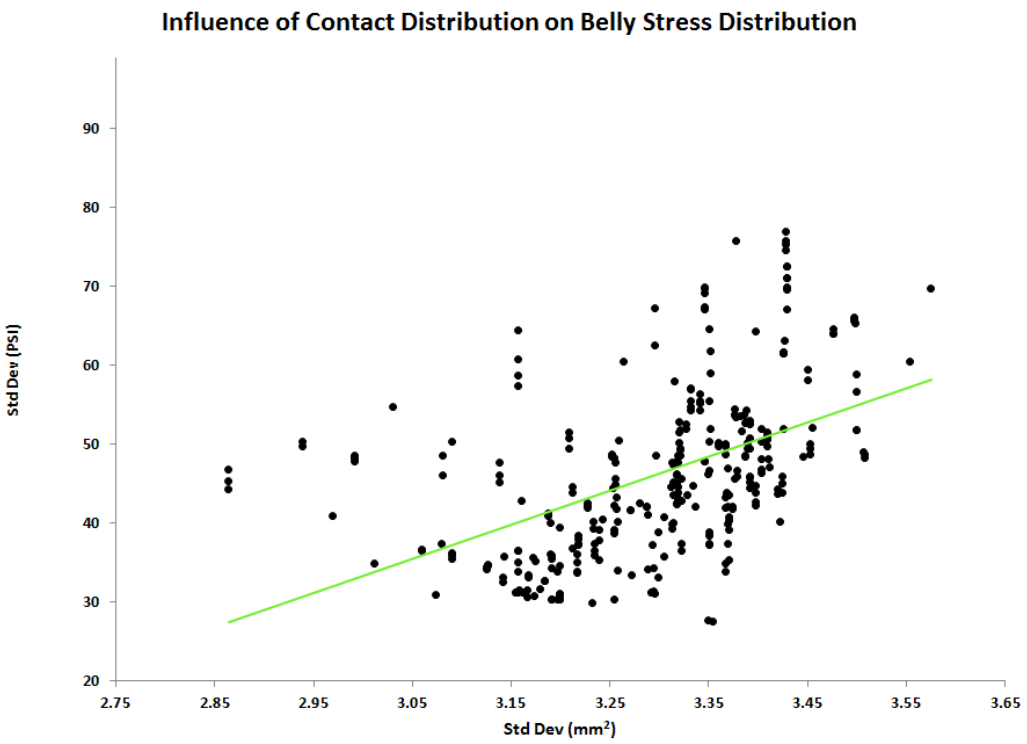

Figure 46. Effect of leaflet contact distribution on stress concentration along the M-region (M_{std}) of the non-collapsing leaflet under E_5 eccentricity optimization. Linear trendline shown in green.

Generally, as contact became more distributed across the leaflet free margin, stress along the belly of the non-collapsing leaflet became more uniform. TAV leaflets normally developed a triangular contact area; however, smoothed coaptation leading to a more rectangular-shaped contact zone tended to produce symmetric stress concentrations which were well spread in the circumferential direction.

3.6 Limitations and Future Directions

Several assumptions were made in this study for simplification. Constant leaflet thickness of 0.24mm was adopted in the computational study. Although BPN and PPK tissues were of similar thickness, it is assumed that the mechanical properties were independent of tissue thickness. Pericardium often exhibits inhomogeneous thickness and

collagen fiber orientation, therefore, future studies may need to analyze the effect of more comprehensive material modeling. Additionally, parameters describing the nominal design represent a generic TAV leaflet and is not a replica of a commercially-available device.

The parameter range represents a moderate design space, but could benefit from expansion to encompass a broader array of geometries. Design could be further parameterized by defining a free edge shape. However, additional input and output parameters increases computational cost, a phenomenon sometimes referred to as the curse of dimensionality. With more design variables, the number of points needed to explore the design space increases rapidly, thus creating a combinatorial explosion. Despite these shortcomings, this study has provided a significant amount of information regarding the leaflet mechanics and the significant role in which geometric optimization may play in TAV durability.

In this study, it was assumed that the peak stress experienced within a typical loading cycle is strongly associated with material fatigue; however, fatigue life of TAV leaflets was not directly predicted. Since mechanical loading is greatest during diastolic closure, valve opening was not modeled in Aim 2. It should be noted that a more comprehensive analysis of TAV durability would include the time-dependent properties of pericardial tissue which can describe the effects of aging and mechanical fatigue damage. Such an investigation would require a significant amount of computational resources; however, the computational framework developed in this work has been used to explore leaflet design and may provide a starting point for the examination of several leaflet geometries.

4 CONCLUSIONS

4.1 Material Properties

Flexure is an important mode of deformation for native and bioprosthetic heart valves; however, characterization of bioprosthetic leaflet materials has been primarily limited to planar biaxial tension. Bovine pericardium has traditionally been selected as the source material for bioprosthetic leaflets due to its ideal mechanical properties. Porcine pericardium is being investigated as an alternative leaflet material due to its exceptional thickness; however, the mechanical properties of porcine tissue have not been well characterized. In this work, it was demonstrated how flexural and biaxial testing can be characterized within a structural constitutive model. The first goal of this study was to investigate potential differences between bovine and porcine pericardium. It was observed that porcine pericardium experienced significantly more flexure than bovine when subjected to TAV pressurization. Interestingly, deflection of thin bovine pericardium was notably greater than that of thick; however, this difference was not as significant in the porcine tissues. The second goal was to determine if biaxial testing alone could accurately model the material response during flexural loading. For the thin pericardial tissues, significant adjustments to the material parameters were required to capture the experimental bending. Thus, it is recommended that a combination of flexural modeling and biaxial tensile testing may be most appropriate when describing the behavior of pericardial soft tissue.

4.2 TAV Leaflet Design

The design of transcatheter aortic valve leaflets was investigated using computational modeling tools. Leaflet geometry was parameterized using mathematical definitions for the free edge, attachment edge, and stent suturing line. Material properties from the experimental characterization of bovine and porcine pericardia were implemented into finite element modeling of a generic TAV leaflet. It was observed that peak stress concentration typically occurred near the attachment edge, below the line of coaptation. Maximum stress experienced in TAV leaflets was consistently correlated with stress distribution across the belly region. This computational study demonstrated how stress distribution may be impacted by leaflet materials. Additional analysis of leaflet deformation revealed that uniformity of contact along the free margin was strongly associated with stress concentration.

The benefit of using computational tools to study the design of sophisticated devices was demonstrated here. Some variables, such as leaflet strain near the stent attachment site, coaptation area, and contact shape cannot be easily measured experimentally. It has been revealed that parameters describing leaflet shape and size may significantly influence these factors in a sophisticated manner. Elegant parameterization lends itself to design exploration and geometric optimization. Optimization of TAV leaflet design was performed for the ideal, circular-deployment state and for several elliptical, misdeployment conditions. As the TAV orifice became more eccentric, leaflet stress increased and geometric optimization was able to mitigate this effect to a significant degree. In this work, a simple form of the leaflet free edge was assumed; therefore, additional work needs to be performed to further reduce TAV leaflet stress and find geometric design which are robust to changes in TAV implantation.

APPENDIX A

Constitutive Modelling

Constitutive model fitting was performed on biaxial testing data for BPK, BPN, PPK, and PPN tissue. The average stress-strain relationship for each of the seven testing protocols and model fitting is shown in Figure 47,Figure 48, Figure 49, and Figure 50.

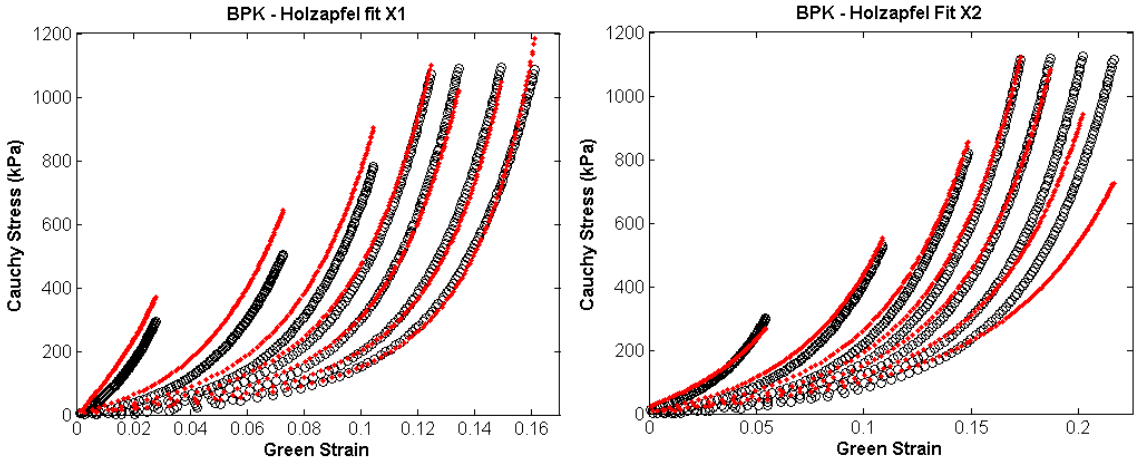

Figure 47. Average biaxial response for thick bovine pericardium in the preferred-fiber (X1) and cross-fiber (X2) directions.

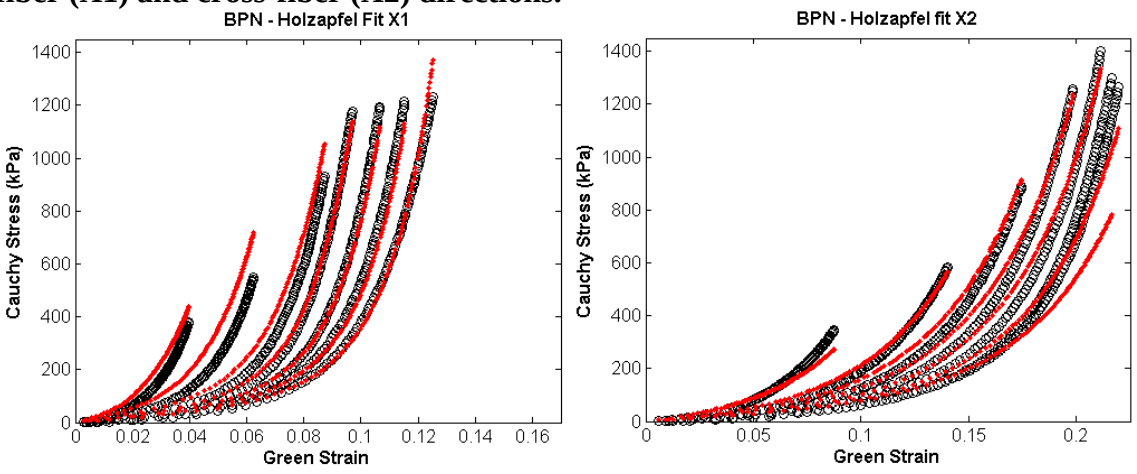

Figure 48. Average biaxial response for thin bovine pericardium in the preferred-fiber (X1) and cross-fiber (X2) directions.

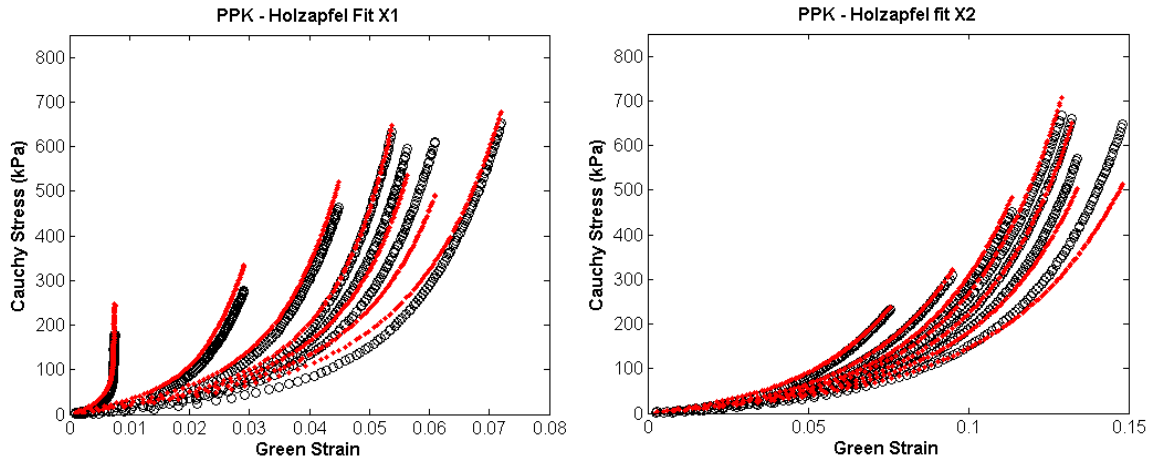

Figure 49. Average biaxial response for thick porcine pericardium in the preferred-fiber (X1) and cross-fiber (X2) directions.

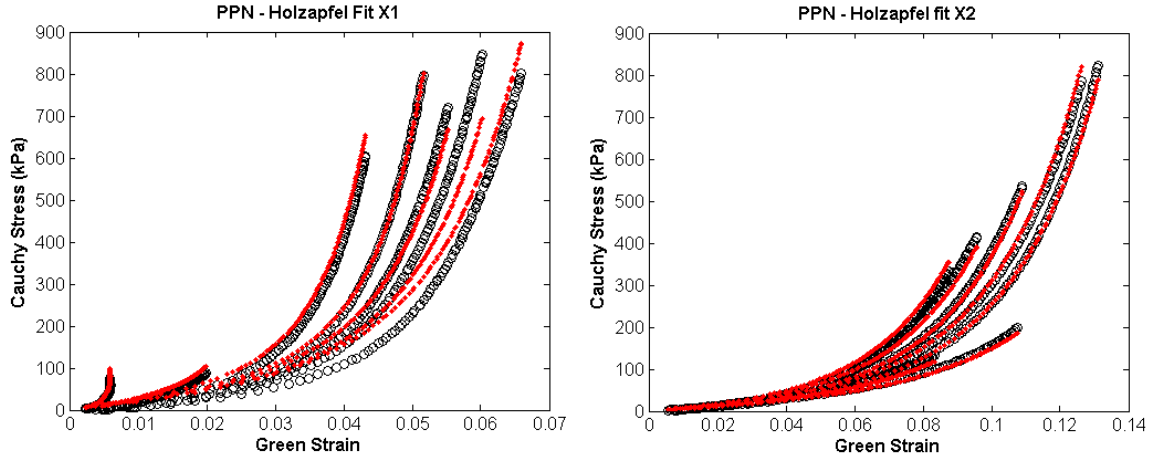

Figure 50. Average biaxial response for thin porcine pericardium in the preferred-fiber (X1) and cross-fiber (X2) directions.

Optimization Histories

The ASA optimization history of BP and PP leaflets are shown in Figure 51 and Figure 52, respectively.

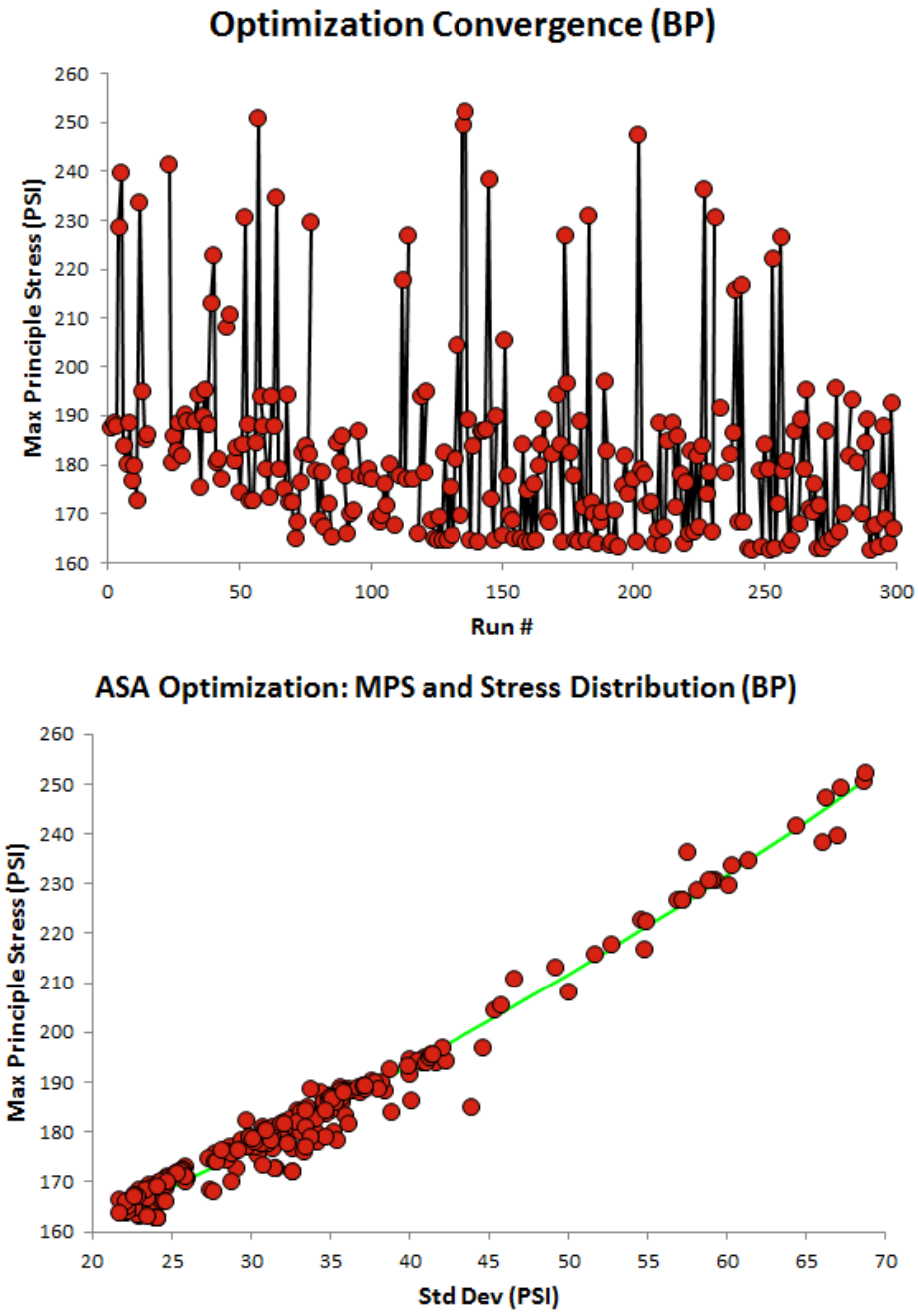

Figure 51. ASA optimization history (top) and relationship between leaflet MPS and M-region stress distribution (bottom) with bovine pericardia properties, trendline shown in green.

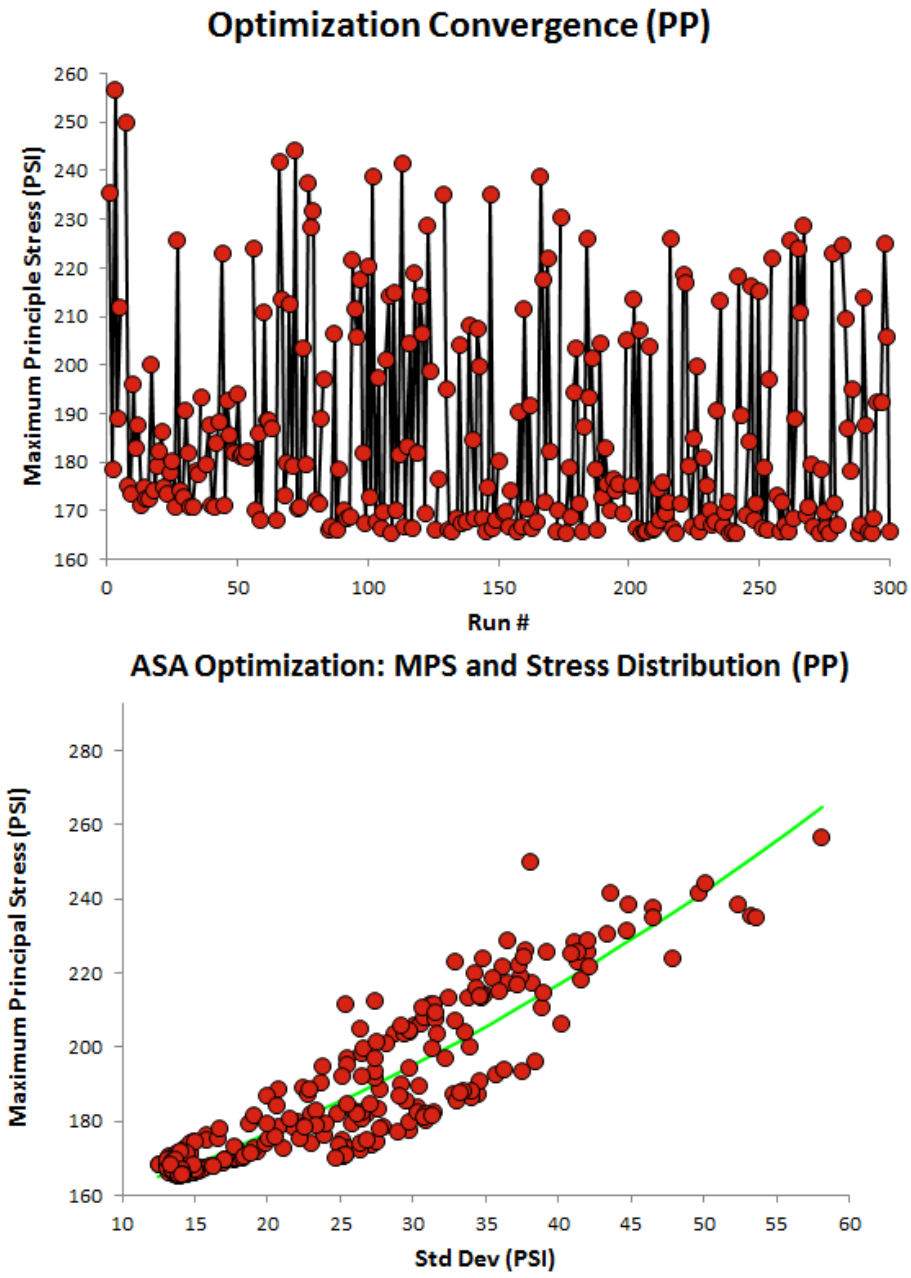

Figure 52. ASA optimization history (top) and relationship between leaflet MPS and M-region stress distribution (bottom) with porcine pericardia properties, trendline shown in green.

REFERENCES

1. Kasel, A.M., et al., *Standardized imaging for aortic annular sizing: implications for transcatheter valve selection.* JACC Cardiovasc Imaging, 2013. **6**(2): p. 249-62.

2. Maganti, K., et al., *Valvular heart disease: diagnosis and management.* Mayo Clin Proc, 2010. **85**(5): p. 483-500.

3. Mozaffarian, D., et al., *Heart Disease and Stroke Statistics-2016 Update: A Report From the American Heart Association.* Circulation, 2015.

4. Thubrikar, M., *The aortic valve*. 1990, Boca Raton, Fla.: CRC Press. 221 p.

5. Thubrikar, M.J., J. Aouad, and S.P. Nolan, *Patterns of calcific deposits in operatively excised stenotic or purely regurgitant aortic valves and their relation to mechanical stress.* Am J Cardiol, 1986. **58**(3): p. 304-8.

6. Back, M., et al., *Biomechanical factors in the biology of aortic wall and aortic valve diseases.* Cardiovasc Res, 2013. **99**(2): p. 232-41.

7. Bach, D.S., *Prevalence and characteristics of unoperated patients with severe aortic stenosis.* J Heart Valve Dis, 2011. **20**(3): p. 284-91.

8. Mack, M.J., et al., *5-year outcomes of transcatheter aortic valve replacement or surgical aortic valve replacement for high surgical risk patients with aortic stenosis (PARTNER 1): a randomised controlled trial.* Lancet, 2015. **385**(9986): p. 2477-84.

9. Cribier, A., et al., *Percutaneous transcatheter implantation of an aortic valve prosthesis for calcific aortic stenosis: first human case description.* Circulation, 2002. **106**(24): p. 3006-8.

10. Zhao, Z.G., et al., *Transcatheter aortic valve implantation in bicuspid anatomy.* Nat Rev Cardiol, 2015. **12**(2): p. 123-8.

11. Martin, C. and W. Sun, *Comparison of transcatheter aortic valve and surgical bioprosthetic valve durability: A fatigue simulation study.* J Biomech, 2015. **48**(12): p. 3026-34.

12. Dvir, D., et al. *First look at long-term durability of transcatheter heart valves: Assessment of valve function up to 10-years after implantation*. in *EuroPCR*. 2016. Paris.

13. Martin, C. and W. Sun, *Simulation of long-term fatigue damage in bioprosthetic heart valves: effects of leaflet and stent elastic properties.* Biomech Model Mechanobiol, 2014. **13**(4): p. 759-70.

14. Aguiari, P., et al., *Mechanical testing of pericardium for manufacturing prosthetic heart valves.* Interact Cardiovasc Thorac Surg, 2016. **22**(1): p. 72-84.

15. Walther, T., et al., *Review: Transcatheter Aortic Valve Implantation.* EMJ Int Cardiol, 2014. **1**: p. 117-123.

16. Fanning, J.P., et al., *Transcatheter aortic valve implantation (TAVI): valve design and evolution.* Int J Cardiol, 2013. **168**(3): p. 1822-31.

17. Schoen, F.J., et al., *Causes of failure and pathologic findings in surgically removed Ionescu-Shiley standard bovine pericardial heart valve bioprostheses: emphasis on progressive structural deterioration.* Circulation, 1987. **76**(3): p. 618-27.

18. Zegdi, R., et al., *Is it reasonable to treat all calcified stenotic aortic valves with a valved stent? Results from a human Anatomic study in adults.* Journal of the American College of Cardiology, 2008. **51**(5): p. 579-584.

19. Sun, W., K. Li, and E. Sirois, *Simulated elliptical bioprosthetic valve deformation: implications for asymmetric transcatheter valve deployment.* J Biomech, 2010. **43**(16): p. 3085-90.

20. Dabiri, Y., et al., *TAVR Valves: The Effect of Post Implantation Leaflet Distortion on Durability.* Cardiology, 2016. **134**(2): p. 221-221.

21. Athappan, G., et al., *Incidence, predictors, and outcomes of aortic regurgitation after transcatheter aortic valve replacement: meta-analysis and systematic review of literature.* J Am Coll Cardiol, 2013. **61**(15): p. 1585-95.

22. Tasca, G., et al., *Impact of prosthesis-patient mismatch on cardiac events and midterm mortality after aortic valve replacement in patients with pure aortic stenosis.* Circulation, 2006. **113**(4): p. 570-6.

23. Matsoukas, G. and I.Y. Kim, *Design optimization of a total hip prosthesis for wear reduction.* J Biomech Eng, 2009. **131**(5): p. 051003.

24. Kowalczyk, P., *Design optimization of cementless femoral hip prostheses using finite element analysis.* J Biomech Eng, 2001. **123**(5): p. 396-402.

25. Kumar, N., *Parametric optimization and design validation based on finite element analysis of hybrid socket adapter for transfemoral prosthetic knee.* Prosthet Orthot Int, 2014. **38**(5): p. 363-8.

26. Dur, O., et al., *Computer-Aided Patient-Specific Coronary Artery Graft Design Improvements Using CFD Coupled Shape Optimizer.* Cardiovasc Eng Technol, 2011. **2**(1): p. 35-47.

27. Chinnakonda, M., et al., *Coronary Stent Design Optimization Using Parametric and Nonparametric Approaches-A Proof of Concept Study.* Journal of Medical Devices-Transactions of the Asme, 2015. **9**(3).

28. Sankaran, S., et al., *Patient-specific multiscale modeling of blood flow for coronary artery bypass graft surgery.* Ann Biomed Eng, 2012. **40**(10): p. 2228-42.

29. Lassila, T., et al., *A reduced computational and geometrical framework for inverse problems in hemodynamics.* Int J Numer Method Biomed Eng, 2013. **29**(7): p. 741-76.

30. Soerensen, D.D., et al., *Introduction of a new optimized total cavopulmonary connection.* Ann Thorac Surg, 2007. **83**(6): p. 2182-90.

31. Wang, Q., et al., *CT image-based engineering analysis of transcatheter aortic valve replacement.* JACC Cardiovasc Imaging, 2014. **7**(5): p. 526-8.

32. Gooley, R.P., J.D. Cameron, and I.T. Meredith, *Assessment of the Geometric Interaction Between the Lotus Transcatheter Aortic Valve Prosthesis and the Native Ventricular Aortic Interface by 320-Multidetector Computed Tomography.* Jacc-Cardiovascular Interventions, 2015. **8**(5): p. 740-749.

33. Willson, A.B., et al., *Structural integrity of balloon-expandable stents after transcatheter aortic valve replacement: assessment by multidetector computed tomography.* JACC Cardiovasc Interv, 2012. **5**(5): p. 525-32.

34. Freed, A.D. and T.C. Doehring, *Elastic model for crimped collagen fibrils.* J Biomech Eng, 2005. **127**(4): p. 587-93.

35. Holzapfel, G.A., *Nonlinear solid mechanics : a continuum approach for engineering*. 2000, Chichester ; New York: Wiley. xiv, 455 p.

36. Fung, Y.C., *Biomechanics : mechanical properties of living tissues*. 2nd ed. 1993, New York: Springer-Verlag. xviii, 568 p.

37. Sacks, M.S. and W. Sun, *Multiaxial mechanical behavior of biological materials.* Annu Rev Biomed Eng, 2003. **5**: p. 251-84.

38. Sun, W., A. Abad, and M.S. Sacks, *Simulated bioprosthetic heart valve deformation under quasi-static loading.* J Biomech Eng, 2005. **127**(6): p. 905-14.

39. Holzapfel, G.A., T.C. Gasser, and R.W. Ogden, *A new constitutive framework for arterial wall mechanics and a comparative study of material models.* Journal of Elasticity, 2000. **61**(1-3): p. 1-48.

40. Gasser, T.C., R.W. Ogden, and G.A. Holzapfel, *Hyperelastic modelling of arterial layers with distributed collagen fibre orientations.* J R Soc Interface, 2006. **3**(6): p. 15-35.

41. Li, K. and W. Sun, *Simulated thin pericardial bioprosthetic valve leaflet deformation under static pressure-only loading conditions: implications for percutaneous valves.* Ann Biomed Eng, 2010. **38**(8): p. 2690-701.

42. Nicosia, M.A., *A theoretical framework to analyze bend testing of soft tissue.* J Biomech Eng, 2007. **129**(1): p. 117-20.

43. Mirnajafi, A., et al., *The effects of collagen fiber orientation on the flexural properties of pericardial heterograft biomaterials.* Biomaterials, 2005. **26**(7): p. 795-804.

44. Cohn, D., et al., *Mechanical behaviour of isolated pericardium: species, isotropy, strain rate and collagenase effect on pericardial tissue* Clinical Materials, 1987. **2**(2): p. 115-124.

45. Luo, X.Y., et al., *Effect of bending rigidity in a dynamic model of a polyurethane prosthetic mitral valve.* Biomech Model Mechanobiol, 2012. **11**(6): p. 815-27.

46. Martin, C. and W. Sun, *Bio-prosthetic Heart Valve Stress Analysis: Impacts of Leaflet Properties and Stent Tip Deflection*, in *SEM Annual Conference*. 2011: Uncasville, CT.